

# **Data Assimilation for Ocean Acoustic Tomography**

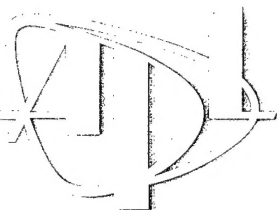
by

C.G. Walter

Technical Report

**APL-UW TR 9901**

July 2000



Applied Physics Laboratory University of Washington  
Seattle, Washington 98105-6898

**ONR Contract N00014-97-1-0259**

**DTIC QUALITY INSPECTED 4**

**20000913 115**

*Approved for public release; distribution is unlimited.*

# **Data Assimilation for Ocean Acoustic Tomography**

by

C.G. Walter

Technical Report

**APL-UW TR 9901**

July 2000



**Applied Physics Laboratory University of Washington**  
1013 NE 40th Street Seattle, Washington 98105-6698

*ONR Contract N00014-97-1-0259*

# Data Assimilation for Ocean Acoustic Tomography

Chris G. Walter

A dissertation submitted in partial fulfillment  
of the requirements for the degree of

Doctor of Philosophy

University of Washington

1999

Program Authorized to Offer Degree: Geophysics

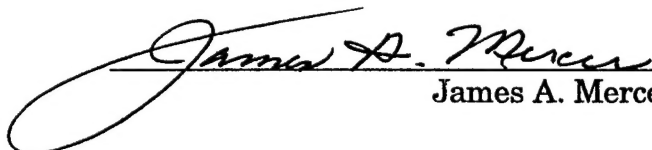
University of Washington  
Graduate School

This is to certify that I have examined this copy of a doctoral dissertation by


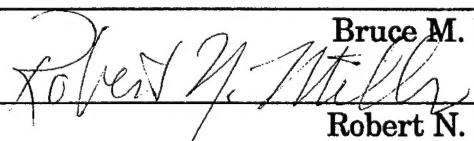
Chris G. Walter

and have found that it is complete and satisfactory in all respects,  
and that any and all revisions required by the final  
examining committee have been made.

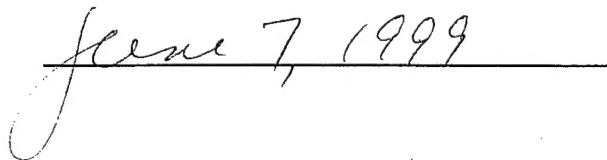
Chair of Supervisory Committee:

  
James A. Mercer

Reading Committee:

  
Bruce M. Howe  
  
Robert N. Miller

Date:



JUL 16 2000





In presenting this thesis in partial fulfillment of the requirements for the Doctoral degree at the University of Washington, I agree that the Library shall make its copies freely available for inspection. I further agree that extensive copying of the dissertation is allowable only for scholarly purposes, consistent with "fair use" as prescribed in the U.S. Copyright Law. Requests for copying or reproduction of this dissertation may be referred to UMI Dissertation Services, 300 North Zeeb Road, P.O. Box 1346, Ann Arbor, MI 48106-1346, to whom the author has granted "the right to reproduce and sell (a) copies of the manuscript in microform and/or (b) printed copies of the manuscript made from microform."

Signature Ch. Y. Walts

Date June 7, 1999

University of Washington

Abstract

## Data Assimilation for Ocean Acoustic Tomography

by Chris G. Walter

Chair of Supervisory Committee

Research Associate Professor James A. Mercer  
Department of Geophysics

This research evaluates the effectiveness of assimilating ocean acoustic tomography data into numerical ocean models. Acoustic tomography uses sound to remotely sample integrated or averaged properties of the ocean. These properties include soundspeed and current velocity. Three different models are used in the assimilation: 1) a linear Rossby wave model without advection, 2) a Rossby wave model with advection, and 3) a non-linear quasi-geostrophic model. We examine the tomographic data's effectiveness by assimilating non-averaging point measurements, such as temperature data, and integral data with the Rossby wave model. First, simulated data are used in benchmark experiments. These are followed by a second series of experiments in which actual tomographic data collected during the Acoustic Mid-Ocean Dynamics Experiment (AMODE) are used. We compare the value of the integral measurements in terms of forecasting accuracy in both physical and spectral space. Although both forms of data constrain the model equally as well in an average sense (the number of data were chosen to do this), the tomographic data are found to constrain low wavenumber components of the model more accurately. Differences between the model estimates and data are within expected error bars. These error bars are based on prior statistical assumptions about errors in the model and observations, boundary conditions and initial conditions. The Rossby wave models with and without advection account for 62.1% and 60.7% of the data variance respectively and the quasi-geostrophic model accounts for

66.0% of the variance. The purpose of this research is not to evaluate any particular numerical model, but rather to better understand the usefulness of assimilating tomographic measurements into numerical models.

## **FOREWORD**

This report is a slightly revised version of the dissertation submitted in partial fulfillment of the requirements for the Doctor of Philosophy degree at the University of Washington in June 1999. Dr. James A. Mercer was the chair of the supervisory committee.

# TABLE OF CONTENTS

<b>List of Figures</b>	<b>iii</b>
<b>List of Tables</b>	<b>iv</b>
<b>Chapter 1: Introduction</b>	<b>1</b>
1.1 Motivation . . . . .	1
1.2 Background . . . . .	3
1.3 Novel Aspects of This Work . . . . .	5
1.4 Thesis Overview . . . . .	6
<b>Chapter 2: Theory</b>	<b>9</b>
2.1 Acoustic Measurements . . . . .	9
2.2 Parameter Estimation and Kalman Filtering . . . . .	12
<b>Chapter 3: Models</b>	<b>17</b>
3.1 Introduction . . . . .	17
3.2 Rossby Wave Model . . . . .	18
3.2.1 Data model . . . . .	20
3.3 Non-Linear Open-Ocean Model . . . . .	21
3.3.1 Introduction . . . . .	21
3.3.2 Theory . . . . .	22
3.3.3 Computational parameters . . . . .	23
3.4 Model Interpolation and Soundspeed . . . . .	25
3.4.1 Comparisons Between Statistical and Dynamic Modes . . . . .	27
<b>Chapter 4: Results</b>	<b>36</b>
4.1 Experiment E1 - Linear Rossby Waves . . . . .	37
4.2 Experiment E2 - Rossby Waves with Advection . . . . .	40

4.3 Experiment E3 - Non-linear HOOM model . . . . .	41
<b>Chapter 5: Discussion</b>	<b>51</b>
5.1 Parameterization . . . . .	52
5.2 Twin Experiments . . . . .	54
5.3 Assimilation Techniques . . . . .	55
5.4 Errors . . . . .	56
5.5 Models and Results . . . . .	57
5.6 Real Data . . . . .	58
<b>Bibliography</b>	<b>62</b>

## LIST OF FIGURES

1.1	Ocean observing systems . . . . .	7
1.2	Block diagram of a twin experiment . . . . .	8
2.1	Vertical Structure . . . . .	15
2.2	Fourier Slice Theorem . . . . .	16
3.1	Regional map showing the AMODE region. . . . .	30
3.2	Mean Surface Eddy kinetic energy . . . . .	31
3.3	Rossby wave parameters . . . . .	31
3.4	Log plot of the <i>a priori</i> model spectrum. . . . .	32
3.5	Schematic of the open ocean QG circulation model. . . . .	33
3.6	Bathymetric Data. . . . .	34
3.7	AMODE Hydrographic data. . . . .	35
4.1	Linear Rossby waves with simulated noisy data . . . . .	43
4.2	Linear Rossby waves with point and tomography data . . . . .	44
4.3	Linear Rossby waves with real data and adaptive Q parameter . . . . .	45
4.4	Non-linear Rossby waves with simulated noisy data . . . . .	46
4.5	Rossby waves with advection . . . . .	47
4.6	Boundary updating only . . . . .	48
4.7	HOOM with boundary Rossby waves and interior updating. . . . .	49
4.8	Quasi-geostrophic energies. . . . .	50

## LIST OF TABLES

3.1	Computational model parameters . . . . .	29
3.2	Percentage of the stream function variance explained by each dynamic and empirical mode. . . . .	29
3.3	Fraction of the variance of the stream function fields which is described by each dynamical mode according to depth. . . . .	30
3.4	Fraction of the variance of the stream function fields which is described by each empirical mode according to depth. . . . .	32
3.5	Cross correlation energies between the empirical and the dynamical modes. . . . .	33



## ACKNOWLEDGMENTS

I wish to expresses my sincere thanks and appreciation to professors Jim Mercer, Robert Miller, and Bruce Howe for their support and assistance. I would also like to express my thanks to Manuel Fiadeiro and the Office of Naval Research for their funding and support. I would especially like to thank my family and especially my wife Jennifer for her patience, encouragement and support in completing this work.

## Chapter 1

# INTRODUCTION

### 1.1 *Motivation*

Measuring and predicting the ocean's mesoscale circulation presents a formidable task for oceanographers. Ocean mesoscale features are comparable to storms and weather fronts in the atmosphere and are of great interest to a wide variety of disciplines, ranging from global meteorology to underwater tracking and submarine detection. In order to measure and adequately resolve these mesoscale features, their length scales must be monitored on the order of the Rossby radius ( $\approx 50$  km in the mid-latitude North Atlantic) and time periods on the order of weeks (Hogg, 1996). This places severe demands on most ocean measurement systems. One system that is particularly efficient at measuring features of this space and time scale is ocean acoustic tomography (Munk and Wunsch, 1979).

With ocean tomography, acoustic pulses are transmitted through the ocean's interior using an array of sources and receivers. The tomographic data consist of travel times or "times of flight". From these travel times, it is possible to deduce the horizontally and vertically averaged soundspeed and currents of the intervening ocean. This averaging makes the measurements integral in nature, and because of this integral nature, the data are more sensitive to eddy and mesoscale features.

Typical non-tomographic measurements consist of in-situ observations such as CTD (Conductivity Temperature and Depth) and XBT (eXpendable BathyThermograph) casts. These forms of data as well as satellite altimetry data can be classified as "point" or non-averaging measurements. (The satellite data actually measure vertical but not horizontal averages of the wa-

ter density). Point measurements, such as these, are sensitive to all horizontal length scales (Cornuelle, 1996). This broad sensitivity makes them prone to contamination from short length scale noise processes (such as internal or gravity waves). Figure 1.1 helps to clarify these concepts. It shows various measurement techniques and the domains over which the measurements integrate or average during the sampling process (aside from any post-processing or smoothing). It is important to note that noise from these non-integrated domains can contaminate the measurements.

In order to best estimate the ocean properties, data assimilation or inverse methods are used to reconstruct the temperature (soundspeed) and current fields from the data. The goal in the assimilation is to take travel time observations that are sparse and possibly contaminated with noise, and produce the best estimate of the ocean's 4-dimensional circulation. Data assimilation is particularly important with data types such as tomography. The non-local nature of tomography can result in significant cross correlations in the properties that tomography is trying to measure (Cornuelle, 1996). If these cross correlations are not properly taken into account, information will be lost or neglected in the model's final estimates. In the past, we simplified this inverse problem by either neglecting the time dependence of the data altogether or by applying some simplified time-lag filter to the data. The interested reader is directed to Munk and Wunsch (1982) or Munk and Wunsch (1979) or Howe et al. (1987). Neither of these approaches makes use of *a priori* knowledge of ocean dynamics to constrain how the temperature and current fields evolve and may produce unrealistic estimates of the circulation.

To help evaluate the success of our assimilation methods, we make use of a number of Twin Experiments (TEs). The two major portions of a TE are a control model and an assimilation estimate of the control model. The assimilation estimate uses data simulated from the control ocean. The control model can be thought of as the "true ocean", and the data as "true" data, which may be artificially contaminated with noise before they are used in the assimilation process. Comparisons are made between the assimilation ocean and the control ocean to measure goodness of the forecasts. See Figure 1.2 which shows a schematic diagram of a typical twin experiment.

In Figure 1.2 we show the four major components that any ocean data assimilation experiment, whether it uses simulated data or real data, consists of: 1) A dynamical model which can evolve an ocean field in time. 2) Observations or data with measurement error, often irregularly sampled in space and time. 3) Error statistics for both the model and the data. 4) A system for combining model output with data. The dynamical model is a form, almost always greatly simplified, of the equations of motion with the necessary initial and boundary conditions. In addition to boundary conditions, measurements in the interior (e.g., current meter data, CTD profiles, acoustic travel times, and drifter positions) are generally used. There are two fundamental data types: point data and integral data. Examples of the first include CTD profiles, pressure data, and current meter data. Examples of integral measurements are acoustic travel time (inverted echo sounders as well as "tomographic" travel times), electric field measurements, drifters and floats, and altimetric sea surface height measurements (height and pressure are functions of the integral of the water density). Float or drifter data are complicated because they are an integral function of time and spatially varying velocity, since they measure  $\int_{t_0}^{t_1} \mathbf{u}(\mathbf{x}(t)) dt$ .

A prescription of the error statistics is absolutely necessary for rigorous data assimilation (Cornuelle, 1996). The data errors may be correlated with one another (such as altimeter orbit errors or XBT fall rate errors), with the model errors, or with the model state itself and may be difficult to estimate. Model errors are especially difficult to prescribe, because doing so usually implies one has a better model available. The specification of errors is often the most difficult (and often subjective) part of data assimilation.

## 1.2 Background

Acoustic tomography was first seriously discussed by Munk and Wunsch (1979, 1982). Munk and Wunsch discuss the wisdom of using information from acoustic transmissions as a means of remotely measuring the ocean mesoscale structure. These acoustic transmissions measure certain properties of the ocean using travel times (times of flight) between distant moorings. By using an array of moorings (actually acoustic transceivers), synoptic collections of "tomographic"

observations may be made over vast regions of the ocean.

Within the last fifteen years numerous tomographic experiments have been conducted in many oceans of the world. Excellent reviews of these experiments are given by Munk et al. (1995) and also by Worcester et al. (1991). In addition, Dushaw et al. (1993) offer a valuable summary of tomographic use of reciprocal travel time transmissions. Even with this proliferation of documentation extolling tomography's value, the oceanography community has shown reluctance in utilizing the data. Partly, the reluctance stems from the drastic difference between point and tomographic data. At this time, the intrinsic value of the tomographic data is not understood or appreciated. Data assimilation may help bring tomographic data into a more acceptable light. This will be achieved by using data assimilation as a tool to learn how the line-integral nature of tomographic data constrains the circulation model. A major goal of this research is to demonstrate the complementary nature of tomographic and point measurements. They should be individual pieces of a total ocean observing system.

Howe et al. (1987) describe a method used to invert travel times for sound-speed and current. These sum and difference travel times measure integral properties of soundspeed (temperature) and current. Tomography's integrating nature acts as a spatial low pass filter, and is more sensitive to low wavenumber features. Cornuelle et al. (1989) and Cornuelle and Howe (1987) have examined these measurement properties for time independent mapping.

The most common data analysis methods that the tomographic community has used to date employ simple linear inverse methods. These inverse methods assume that all travel time data is collected over a fixed time window. Several tomographic researchers have tried limited variations on this theme. For example, Howe et al. (1987) applied a simple time-lag filter using travel times which were collected with a single source-receiver pair. Spiesberger Metzger (1989) analyzed data by using a generalized mapping method with a time and space varying covariance function. Neither method considered any knowledge of ocean circulation dynamics to constrain the temperature or current fields. Several analysis methods, e.g., those by Chiu and Desaubies (1987) and Cornuelle et al. (1985) use simple linear dynamics. These dynamics assume the

model perturbations are linear Rossby waves with time-independent amplitudes.

The term “data assimilation” stems from the meteorological field. About 40 years ago, the phrase was coined as a method of combining observations with numerical models to improve forecasting accuracy. To do this, observations at a prescribed time are melded with model predictions to estimate new initial conditions. These new initial conditions are then in turn used in the next forecast run. The development of assimilation methods which are used in physical oceanography has always lagged behind meteorology by several years. There is no technical reason for this lag since both fields use the same general-circulation models which have the same level of complexity. A lack of adequate oceanographic data sets has been cited as the likely reason for the lag (Miller et al., 1997). The meteorologists have several orders of magnitude more data at their disposal than the oceanographers. A sobering statistic: the total number of recorded oceanographic *in situ* observations, over the last 100 years or so, would only fill 2.4 gigabytes.

Many approaches have been used to assimilate data into comparatively complex ocean models using an ad hoc scheme in which the observational data “nudges” the model toward the measurement (Malanotte-Rizzoli and Holland, 1986). The nudging methods fall into a class similar to that of direct data insertion. These simple assimilation methods do not allow for the non-local nature of the measurements themselves and neglect the off-diagonal terms of the model error covariance and data covariance. Gaillard (1992) performed a twin experiment using a two mode QG model. Point and tomographic data were simulated and used to reconstruct the stream function fields using simple time-independent inversions. Although the first baroclinic mode was adequately resolved, the barotropic mode was not.

### **1.3 Novel Aspects of This Work**

This work presents the results of assimilating tomographic sum and reciprocal travel time measurements into a linear Rossby Wave model, a non-linear Rossby Wave/Advection model and a quasi-geostrophic open ocean circulation model. A Kalman filter and various sub-optimal updating schemes were used.

Twin experiments are first used to evaluate the information content in the assimilations. Actual AMODE sum and reciprocal travel times (The AMODE-MST Group, 1994) are then assimilated using these models. Energy statistics for the AMODE region are presented.

#### **1.4 Thesis Overview**

The balance of this thesis is divided into four chapters in which we discuss numerical experiments involving point and tomographic data, and the assimilation of the AMODE travel time data using three different models.

We begin by discussing the theory of ocean acoustic tomography and the theory of parameter estimation using Kalman filtering in Chapter 2.

Next, Chapter 3 outlines the models used to fit the tomographic measurements. These models vary in their complexity and include a linear Rossby wave model, with and without advection, in addition to a non-linear open ocean circulation model.

Chapter 4 discusses the results of the parameter estimation. It is divided into three major experiments, E1, E2, and E3. The first portions of E1 and E2 discuss results from numerical experiments, and the second portions of E1 and E2 and E3 discuss results of fitting real AMODE travel time data.

Finally, in Chapter 5 we discuss the findings of this thesis and offer opportunities for future research directions.

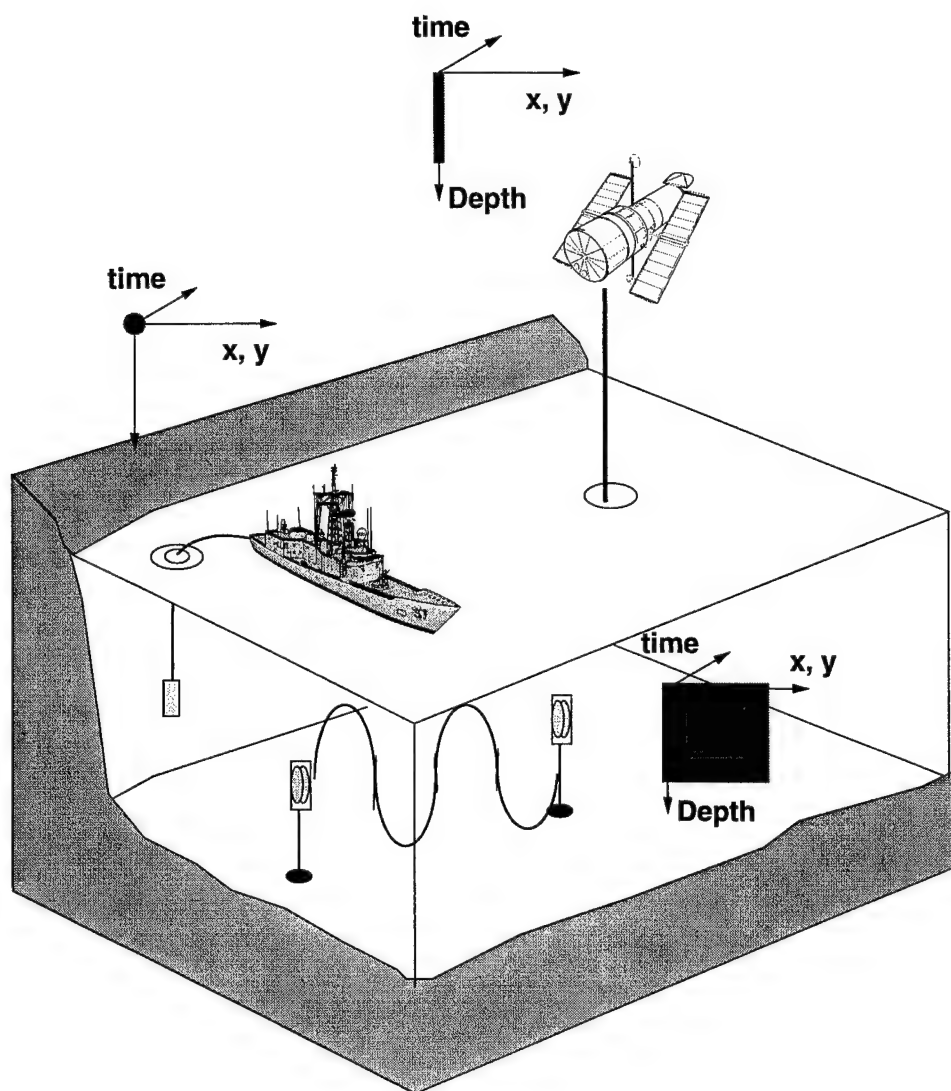


Figure 1.1: As part of a larger ocean observational system, acoustic tomography would be combined with other forms of ocean measurements, such as ship based CTD and satellite altimeter data. Its integral and synoptic properties help it to complement these other measurements.



### Twin Experiment Block Diagram

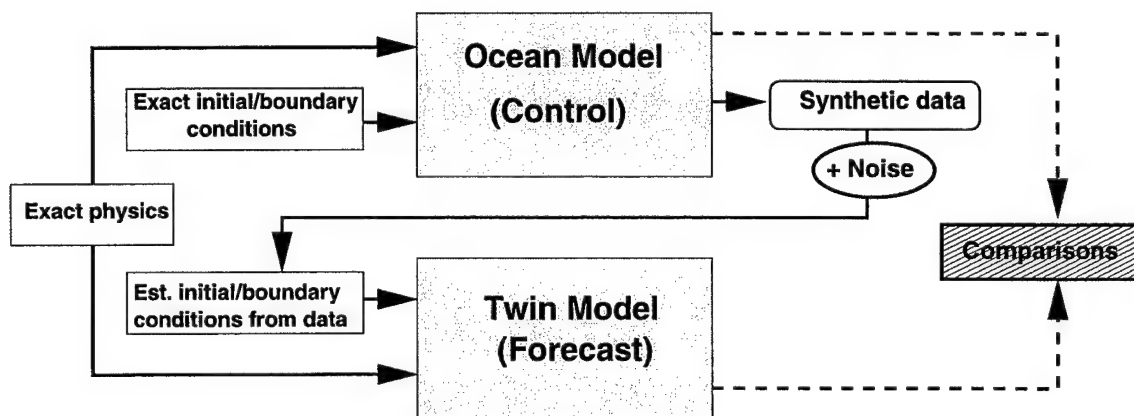


Figure 1.2: Block diagram of a twin experiment

## Chapter 2

### THEORY

This chapter discusses the theory of acoustical tomography travel time measurements as well as parameter estimation. By no means is this an exhaustive discussion; it simply covers the main topics of these subjects that are germane to this research.

#### **2.1 *Acoustic Measurements***

As discussed in Chapter 1, the sampling properties of tomographic data are quite different from those of point data. Ray theory provides a relatively simple yet complete means of explaining acoustic propagation for most tomographic applications. It can generally be used when the acoustic energy is not scattered or absorbed by the ocean's surface or bottom. The AMODE experiment was conducted in deep enough water (~5000 m), and the sources used high enough frequency (250 Hz), that ray theory can be used to model the acoustic measurements.

Using ray theory, we can view the propagation of acoustic energy between a source and a receiver as being a summation of multipaths. A multipath is an eigenray which satisfies Snell's law and intersects the source and receiver. Each path is slightly different from the next; an acoustic pulse that originates at the source will require a slightly different travel time to complete the journey to a given receiver.

The refraction of the acoustic paths is primarily controlled by the vertical soundspeed gradient, and effects of currents can be ignored when tracing the rays. An average soundspeed curve for the AMODE region is shown in Figure 2.1, Panel A. This soundspeed curve was derived using yearly averaged Levitus hydrographic data taken within the AMODE region (Levitus, 1982). The soundspeed minimum (which for this region is at a depth of about 1200 m) acts

as a geometrically dispersive wave guide or “sound channel”. If the source and receiver pair are positioned near the axis of this minimum, the ray paths will “oscillate” around the minimum axis, with turning points above and below the axis (See Panel B of Figure 2.1).

As Figure 2.1 shows, each ray has a number of turning points. The horizontal distance between two adjacent, upper or lower, turning points is called the double loop length. Typically, in the AMODE region this distance is on the order of 30 km for low angle rays and about 80 km for steeper angle rays. The turning depths and the double loop length of the ray primarily determine the spatial sampling properties of the raypath. These sampling properties include the depth resolution and limited horizontal resolution of the raypath.

The travel time path integral gives the time of flight for an acoustic pulse along a given ray path. This equation represents the measured travel time  $T$  of the  $i$ th raypath between the source and receiver pair.

$$T_i = \int \frac{ds}{c_0(\mathbf{x}) + \delta c(\mathbf{x}, t) + \mathbf{u}(\mathbf{x}, t) \cdot \boldsymbol{\tau}} + \epsilon_T \quad (2.1)$$

where  $ds$  is the incremental path length,  $t$  is geophysical time,  $c_0(\mathbf{x})$  is a reference soundspeed,  $\delta c(\mathbf{x}, t)$  is perturbation soundspeed and  $\mathbf{u}(\mathbf{x}, t) \cdot \boldsymbol{\tau}$  is the component of the three-dimensional current velocity along the raypath. The noise term  $\epsilon_T$  has been added to represent instrument error, internal wave noise, etc. The travel times may be summed and differenced between sources and receivers in each direction in order to estimate  $\delta c(\mathbf{x}, t)$  and  $\mathbf{u}(\mathbf{x}, t)$ . After linearizing this equation about the reference soundspeed  $c_0(\mathbf{x})$  and forming sum and differences of forward (+) and reciprocal (-) perturbation travel times  $\delta T$ , we get:

$$\begin{aligned} \frac{\delta T_i^+ + \delta T_i^-}{2} &= - \int_{\Gamma_i} \frac{\delta c(\mathbf{x}, t)}{c_0(\mathbf{x})^2} ds + \epsilon_+ \\ \frac{\delta T_i^+ - \delta T_i^-}{2} &= - \int_{\Gamma_i} \frac{\mathbf{u}(\mathbf{x}, t) \cdot \boldsymbol{\tau}}{c_0(\mathbf{x})} ds + \epsilon_- \end{aligned} \quad (2.2)$$

An implicit assumption made in this linearization is that the perturbations in

soundspeed  $c_0(z)$  are sufficiently small that they do not modify the raypath  $\Gamma_i$  (the frozen field assumption). For soundspeed fields encountered in this research, the non-linear effects in travel time are estimated to be on the order 0.1 ms, which is considerably less than the noise level of the data,  $\epsilon$ . The additive noise term,  $\epsilon_+$ , represents the combined noise terms which may result from unmodeled mooring motion, clock drift, internal wave noise, just to name a few. And  $\epsilon_-$  contains primarily errors resulting only from clock drift.

In order to invert the travel time data, the time series of measurements needs to be carefully matched or aligned to the respective predicted eigenrays,  $\Gamma_i$ . The modeled acoustic rays were aligned with the data by matching patterns in the arrival times and vertical arrival angles. The end product of this arrival matching process identified about 15 arrivals for each source and receiver pair. For this study, three rays per source and receiver pair were used, an axial, steep, and an intermediate turning ray. It was determined that vertical resolution is diminished negligibly by using only a subset of the ray paths.

It is convenient to think of tomography as building an image, in a sequence, of vertical and horizontal slices (Kak and Slaney, 1988). The previous sections discussed factors affecting the vertical resolution; now we will examine how the map or model may be resolved in the horizontal slice. The Fourier slice theorem tells us that the Fourier transform of a projection is equivalent to the Fourier transform of the image along a given radial  $\theta$ .

Figure 2.2 shows a simple tomographic geometry and diagrams the Fourier slice theorem. It shows that in order to build up the image in Fourier space, multiple projections at different  $\theta$ 's need to be made. Once the image is built in wavenumber space, its equivalent can be obtained in physical space by using an inverse transform.

In Chapter 3, we will parameterize the soundspeed perturbation,  $\delta c$ , and current variability,  $\mathbf{u}(\mathbf{x}, t)$ , as a set of harmonics  $S(\mathbf{k})$  ( $\mathbf{k}$  is the wavenumber ordinate, and  $\mathbf{x}$  the physical space ordinate). We will show that the sum travel time perturbations from Equation 2.2 can be re-written as:

$$\delta T_+ = \int_{\Gamma_i} \frac{\int Z_c(z) S(\mathbf{k}) \exp[-i\mathbf{k} \cdot \mathbf{x}] d\mathbf{k}}{c_0^2(z)} ds .$$

And the difference travel times are given by:

$$\delta T_- = \int_{\Gamma_i} \frac{\int Z_\psi(z) S(\mathbf{k}) (i \nabla_x \exp[-i \mathbf{k} \cdot \mathbf{x}]) \cdot \tau d\mathbf{k}}{c_0(z)} ds .$$

The complex amplitudes  $S(\mathbf{k})$  are the Fourier components of the stream function field.

## 2.2 Parameter Estimation and Kalman Filtering

The overall goal of parameter estimation is to optimally (what is optimal will be defined shortly) fit a set of model parameters,  $x_k$ , to a set of noisy measurements. These parameters evolve between measurement times according to uncertain dynamical laws. Further, some or all of the measurements and dynamical transition functions may be nonlinear, i.e., functions with non-constant derivatives.

More formally, the problem is to estimate the state sequence  $x_k$ , where  $x_k$  is a state vector of dimension  $m$  for each time step  $k$ . We are given a series of vector valued measurements (say travel times),  $z_k$ , as well as an estimate of the initial state,  $\hat{x}_0$ . Further, let  $n(k)$  be the dimension of the data space for the  $k$ th time step.

We can then relate the data vector,  $z_k$ , to the state values using a measurement equation

$$z_k = h_k(x_k) + v_k , \quad (2.3)$$

where  $h_k$  represents a noiseless measurement functional and  $v_k$  is the noise term which is normally distributed with mean zero and variance  $R_k$ . We assume that the functions  $h(k)$  and  $R_k$  are known *a priori*.

Now a transition equation can be written which relates the state estimate at each time point to the state values at a previous time point:

$$x_k = \phi_k(x_{k-1}) + w_k , \quad (2.4)$$

where  $\phi_k$  represents the noiseless transition and  $w_k$  is normally distributed with mean zero and variance  $Q_k$ . We assume that the function  $\phi_k$  and variance  $Q_k$  are known. The initial estimate of the state  $\hat{x}_0$  is related to the true initial by

$$x_0 = \hat{x}_0 + e_0 ,$$

where  $e_0$  is normally distributed with mean zero and known variance  $P_0$ .

We assume the all the noise variances are uncorrelated and are positive semi-definite (no negative eigenvalues). The cost function,  $J$ , is defined as the negative log likelihood function for our problem and is given by:

$$\begin{aligned} J(x_0, x_1, \dots, x_N) = & (x_0 - \hat{x}_0)P_0^{-1}(x_0 - \hat{x}_0)^T \\ & + \sum_{k=1}^N (z_k - h_k(x_k))R_k^{-1}(z_k - h_k(x_k))^T \\ & + \sum_{k=1}^N (x_k - \phi_k(x_{k-1}))Q_k^{-1}(x_k - \phi_k(x_{k-1}))^T . \end{aligned} \quad (2.5)$$

The optimal estimate for  $x_k$  will be the one which minimizes the cost function. The particular method used to find the minimization is highly problem dependent. For instance, when all of the measurement and transition functions are affine (constant derivative), an ordinary least squares method can be used which takes advantage of the "uncoupled" nature of the measurements and transition processes. This method is known as the Kalman filter or Kalman smoother (the affine smoother is a Kalman filter with a backwards solution enhancement portion).

It can be shown that the Kalman smoother/filter in effect makes successive transformations of the minimization problem for  $J$  at each time step,  $k$ . Each minimization corresponds to a step in the filter or smoother. We will simply state the results of the transformation; the interested reader is referred to Bell (1994) for the proof. The first portion of the transformation is composed of the least squares update theorem:

$$\begin{aligned} \hat{x} &= x + K(z - h(x)) \\ \hat{P} &= (I - KH)P \\ K &= PH^T S^{-1}, \quad S = (HPH^T + R) . \end{aligned}$$

For convenience, we have omitted the subscripting for the time step, and we have introduced the following terms:  $\hat{x}$  is the state estimate (at the  $k$ th time step) derived from  $x$  the forecast model estimate.  $K$  is the Kalman “gain”, which pre-multiplies the “residual”, i.e., the difference between  $z$  (the observations) and  $h(x)$  (the forecast estimate of the observations at the  $k$  th step).  $\hat{P}$  is the estimated covariance of the state estimate,  $I$  is the identity matrix,  $H$  is the gradient (with regard to  $x$ ) of the measurement functional  $h$ , and  $P$  is the forecast covariance (which is discussed next).

In order to propagate the state estimate and its covariance ( $\hat{x}$  and  $\hat{P}$ ) to the next time step, we use the transition step

$$\begin{aligned} P &= \Phi \hat{P} \Phi^T + Q \\ x &= \phi(\hat{x}) , \end{aligned}$$

where we have introduced the new term  $\Phi$  which is the  $m \times m$  transition matrix composed of the gradient of  $\phi$  with regard to each of the model parameters  $x$ . This algorithm is collectively known as the Kalman filter and will be used as an estimation method for the models discussed in the following chapter.

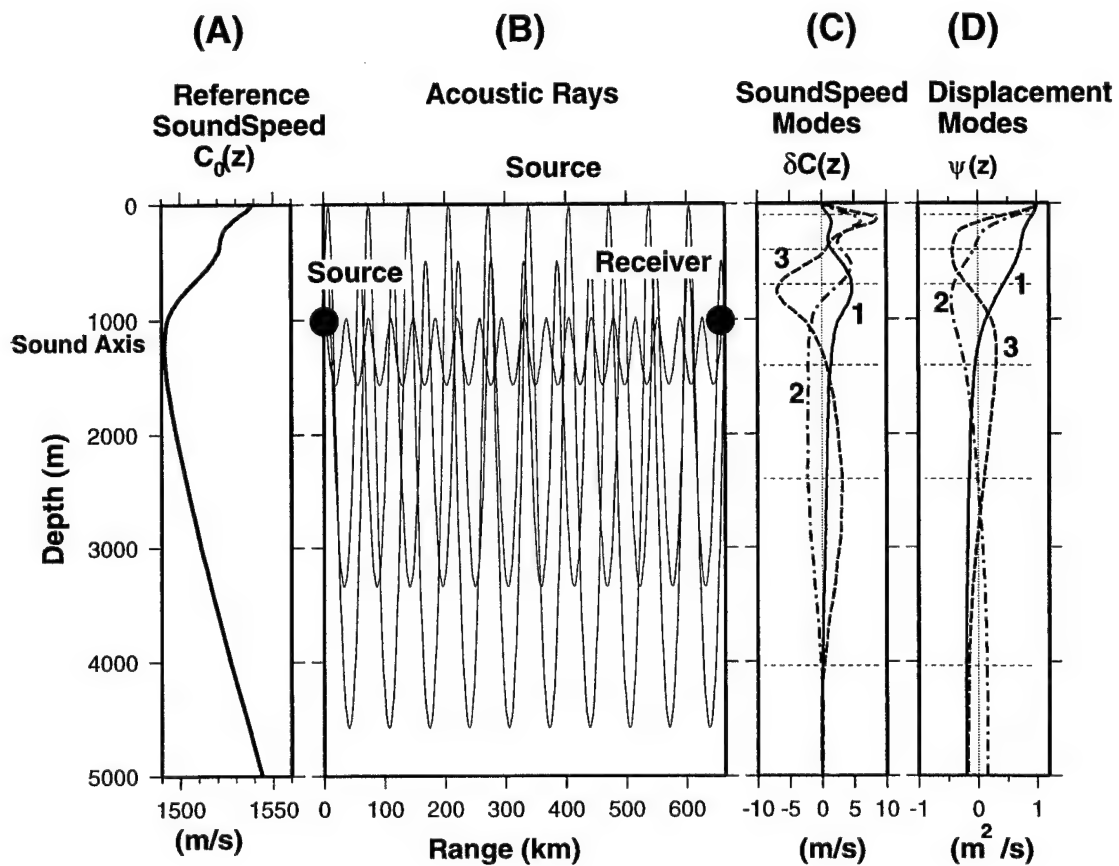


Figure 2.1: Panel A shows the reference soundspeed used in the ray trace. Panel B shows a sample of three rays for a 650 km path, and Panels C and D show the vertical eigenmodes of soundspeed and stream function used in the modeling.



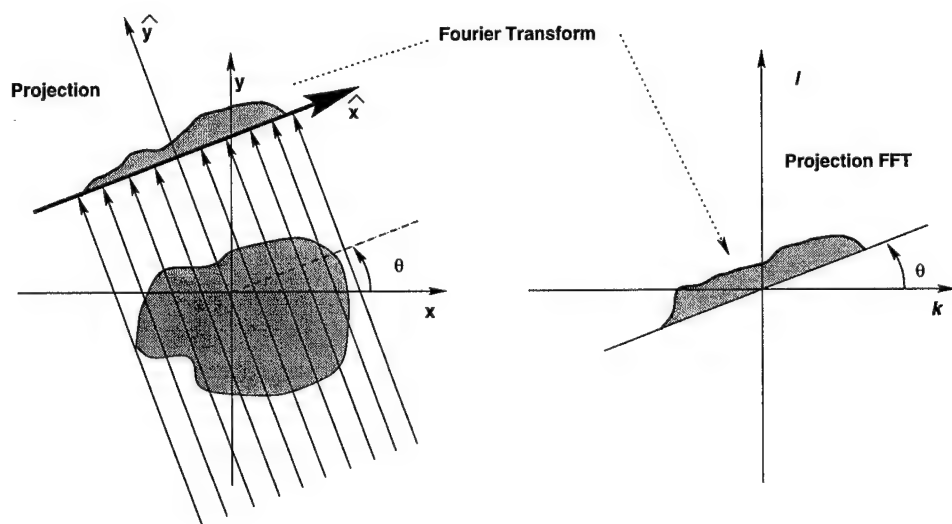


Figure 2.2: Fourier Slice Theorem used in tomography (after Kack and Slaney, 1988).

## Chapter 3

### MODELS

#### 3.1 *Introduction*

This work is designed after and uses data collected from the AMODE experiment, which assembled a tomographic array of six acoustic transceivers moored to the ocean's bottom in a pentagonal array (Dushaw et al., 1996). The array was located between Puerto Rico and Bermuda (See Figure 3.1). The AMODE experiment actually consisted of several experiments. The moored portion collected a long time series of sum and difference travel time data as well as point temperature data at three depths along each of the moorings. Another portion consisted of a high-resolution moving ship tomography experiment, which collected one-way travel time data between the moorings and a ship circumnavigating the perimeter of the array. A third portion consisted of verification data collected from CTD surveys conducted in the moving ship tomography experiment and two additional AXBT surveys. This work will utilize a limited portion of the AMODE data, that from the moored transceivers.

The ranges between the moorings were nominally 350, 410, and 660 km, and the resulting series of travel time measurements covered 180-300 days with sampling occurring every 4 hours on every 4th day. All of the travel time data was high-pass filtered prior to analysis by B. Dushaw in order to remove daily (tidal) variability.

The AMODE region lies to the south of the Gulf Stream recirculation zone. The MODE Group (1978) studied the area slightly to the north and determined that that quasi-geostrophic dynamics could be used to model the region, and that geostrophy and non-divergence are established to within 10%. Figure 3.2 shows the mean kinetic energy (Wyrтки et al., 1976) for the region as well as other primary oceanographic features for the area.

### 3.2 Rossby Wave Model

In this section, we will develop the non-linear Rossby wave model which is complete with advection. The linear version with no advection follows trivially by setting the advection to zero.

Rossby waves, also called planetary waves, rely in part on the earth's curvature (i.e., the variation of Coriolis force with north-south distance) for their existence. Rossby waves are solutions to the potential vorticity equation with no forcing. We can separate the solution into horizontal and vertical parts. This separation allows us to parameterize the solution for the stream function by using a smooth superposition of spectral functions in the horizontal and quasi-geostrophic modes,  $Z_l(z)$ , in the vertical. These modes are solutions to the vertical portion of the quasi-geostrophic equation with flat bottom and free surface boundary conditions.

The horizontal modes are simple sines and cosines, so we can express the stream function,  $\psi(\mathbf{x}, z, t)$ , as a summation of complex wave amplitudes,  $S_{j,l}$ , and vertical functions,  $Z_l(z)$ :

$$\psi(\mathbf{x}, z, t) = \sum_{j,l} Z_l(z) S_{j,l} \exp(i(\mathbf{k} \cdot \mathbf{x} - \omega_{j,l} t)) , \quad (3.1)$$

where we have summed over the  $j$  horizontal and  $l$  vertical modes. The wave frequency,  $\omega$ , controls the time dependence of the waves and must satisfy the dispersion relationship. The dispersion relationship is found by constraining the waves to satisfy the vorticity equation, which will be discussed in Section 3.3.2. After doing so, we find that for a fluid with advection,  $\omega$  has the form

$$\omega = -\frac{k}{K^2 - \lambda_l^2} - \Delta\omega_a$$

where  $K^2 = k^2 + l^2$ , and we have introduced  $\lambda_l$  which is an eigenvalue from the solution to Poisson's equation shown in Equation 3.9. The term  $\Delta\omega_a$  is the portion of the dispersion relationship caused by the horizontal advection velocity for each of the modes.

We will use  $U_1$  for the advection velocity of the barotropic mode, and  $U_2$  for

the advection velocity of the baroclinic mode. We find that  $\Delta\omega_a$  for the first two modes is equal to:

$$\begin{aligned}\Delta\omega_{a,1} &= -\mathbf{U}_1 \cdot \mathbf{k} \\ \Delta\omega_{a,2} &= -2\mathbf{U}_1 \cdot \mathbf{k} - \frac{\mathbf{U}_2 \cdot \mathbf{k} \epsilon K^2}{K^2 - \lambda_2^2}.\end{aligned}$$

For the linear Rossby wave model,  $\mathbf{U}_1$  and  $\mathbf{U}_2$  are zero and we can omit the  $\Delta\omega$  terms from the dispersion formula.

A diagram showing the wave parameters,  $S_{j,l}$ , in the complex plain is shown in Figure 3.3. The harmonics  $S_{j,l}$  are two-dimensional Fourier harmonics in a box, which must contain the data array but can be any size. If the domain of the harmonics is the same as the domain of the data, then the periodicity of the expansion functions will be enforced in the inverse. In the experiments involving numerical simulations of data, the data is periodic so that no discontinuities are present even though the data and model domain sizes coincide. In the assimilation runs using real data, the model domain was chosen to be two times as large as the data domain, in order to avoid Gibbs effects (Cornuelle et al., 1989).

The *a priori* energy spectrum in the model,  $\hat{P}$ , is assumed to be “red”, i.e. homogeneous and isotropic, monotonically decreasing with increasing scalar wavenumber (Wunsch, 1983). For these experiments we have assumed the functional form for the spectral power to be:

$$\hat{P}(K) = \frac{1}{1 + \left(\frac{K}{K_s}\right)^2},$$

where  $K = \sqrt{k^2 + l^2}$ , and we use  $K_s$  as a parameter to set the half power point “shoulder point” for the spectral power. Figure 3.4 shows the spectrum of the *a priori* covariance.

The Kalman filter requires specification of the model noise covariance  $Q$ . For this research, we have chosen to use a scaled version of the *a priori* covariance,  $P_0$ , which relaxes to zero with a time scale,  $\tau$  (Howe et al., 1987). This assumes that  $P_0$  specifies the climatological variances from the reference state.

$Q$  then may be written as:

$$Q(\delta t) = P_0\left(\frac{\delta t}{\tau}\right) \quad t < \tau$$

$$= P_0 \quad t \geq \tau .$$

The time scale,  $\tau$ , was chosen to be approximately 300 days. We will now discuss the measurement model for the travel time data.

### 3.2.1 Data model

The tomographic data which consists of the sum and reciprocal travel times between moorings can be expressed as:

$$z_n(t) = \sum_{j,l} H_{n,j,l} S_{j,l} \exp[-i\omega_{j,l}(\mathbf{U})t] \quad (3.2)$$

where  $z_n(t)$  is the  $n$ th travel time datum at the time step  $t = t_k$ .  $H_{n,j,l}$  is the measurement functional that maps each complex wave amplitude,  $S_{j,l}$ , to a particular travel time datum. For this research we used 15 source receiver pairs each having 3 eigenrays (45 sum travel times and 45 reciprocal travel times).

The gradients of Equation 3.2 with respect to the model parameters  $S$  and  $\mathbf{U} = [u_1, v_1, u_2, v_2]$  are:

$$G = \frac{\delta z_n(t)}{\delta S_{j,l}} = H_{n,j,l} \exp[-i\omega_{j,l}(\mathbf{U})t] \quad (3.3)$$

$$\frac{\delta z_n(t)}{\delta u_1} = \sum_{j,l=1} -(ikt)S_{j,l}G + \sum_{j,l=2} -(2ikt)S_{j,l}G \quad (3.4)$$

$$\frac{\delta z_n(t)}{\delta v_1} = \sum_{j,l=1} -(ilt)S_{j,l}G + \sum_{j,l=2} -(2ilt)S_{j,l}G \quad (3.5)$$

$$\frac{\delta z_n(t)}{\delta u_2} = \sum_{j,l=2} \frac{-ikt\epsilon K^2}{K^2 - \lambda_2^2} S_{j,l}G - H_{n,j,l} \cdot x \quad (3.6)$$

$$\frac{\delta z_n(t)}{\delta v_2} = \sum_{j,l=2} \frac{-ilt\epsilon K^2}{K^2 - \lambda_2^2} S_{j,l}G + H_{n,j,l} \cdot y . \quad (3.7)$$

Note that for the linear Rossby wave model,  $\mathbf{U} = 0$ , and the above equation

simplifies to:

$$\frac{\delta z_n(t)}{\delta S_{j,l}} = H_{n,j,l}.$$

For the non-linear case, the additional terms in Equation 3.3 must be evaluated. We will now discuss the non-linear circulation model, after which we will return to discussion of the Rossby wave models again. The assimilation results are given in Chapter 4.

### **3.3 Non-Linear Open-Ocean Model**

#### *3.3.1 Introduction*

Within the last few years, the ocean modeling community has made great strides and advances. Their efforts have led to an unprecedented variety of complexity in ocean circulation models (Holland and Capotondi, 1996). Some models, such as those that couple the circulation of the atmosphere and global oceans, are very complex and require a great deal of computational resources. Others, such as single-layer gravity-wave models, are more simplistic and require relatively meager computational resources. Quasi-geostrophic (QG) models fall at about the midpoint of this spectrum. QG models use a simplified set of equations to describe the motion of large-scale and meso-scale features. These motions result from slight force imbalances that exist between the geostrophic pressure gradients and coriolis forces (Apel, 1987). The pressure gradients are directly related to horizontal gradients in the water density.

This study uses a QG model known as the Harvard Open Ocean Model or HOOM (Miller et al., 1983). HOOM belongs to a class of circulation models known as regional or "open ocean" circulation models. Regional models do not use explicit boundaries or coast lines to contain the circulation model. Implicit or computational boundaries are used to communicate or interact with the flow regions outside the model domain. Since the modeling domain need not encompass an entire ocean basin, the regional model's horizontal resolution may be fine enough to resolve mesoscale features (order 50 km). This boundary communication involves specifying boundary conditions along the perimeter of the model. The boundary information is only specified along inflow segments of the

boundary; the outflow is prescribed by the interior flow field of the model.

Many researchers have used HOOM in a variety of assimilation and modeling studies. Rienecker and Miller (1991) used the model to investigate the California Current, while Pinardi and Robinson (1987) used the model in the POLYMODE region. Haidvogel et al. (1980) originally developed HOOM as a barotropic model, and HOOM was later configured into a baroclinic version by Miller et al. (1983).

### 3.3.2 Theory

The HOOM model integrates the quasi-geostrophic equations of motion on a beta plane. The potential vorticity,  $\zeta$ , with forcing  $F$  is integrated level by level according to the equation

$$\left[ \frac{d}{dt} + \epsilon_\beta J(\psi, \cdot) \right] \zeta + \beta \frac{\delta \psi}{\delta x} = F. \quad (3.8)$$

The stream function,  $\psi$ , is solved as a function of the potential vorticity using the Poisson equation:

$$\nabla^2 \psi + \Gamma^2 (\sigma \psi_z)_z = \zeta, \quad (3.9)$$

where  $J$  is the Jacobian operator defined as

$$J(A, B) = \frac{\delta A}{\delta x} \frac{\delta B}{\delta y} - \frac{\delta B}{\delta x} \frac{\delta A}{\delta y}, \quad (3.10)$$

and the following terms are defined as

$$\epsilon_\beta = \frac{V_0}{\beta d^2},$$

$$\beta = \frac{2\Omega}{a} \cos \Theta, \quad (3.11)$$

$$\Gamma = \frac{f_0 D}{N_0 h_T}, \quad (3.12)$$

$$\sigma(z) = \frac{N_0^2}{N(z)^2}, \quad (3.13)$$

$$N(z)^2 = \frac{g}{\rho_0} \frac{\delta \rho}{\delta z}. \quad (3.14)$$

Table 3.1 describes all the variables introduced in the above equations, and lists the numerical values for the model parameters.

The stream function,  $\psi$ , is directly related to the pressure anomaly using the relationship

$$p = \rho_0 f_0 \psi. \quad (3.15)$$

The density anomaly,  $\delta$ , is often used as a variable that is assimilated. It may be derived from  $\psi$  by applying the hydrostatic equation. We merely state the result as

$$\delta = \Gamma^2 \sigma \frac{\delta \psi}{\delta z}. \quad (3.16)$$

The numerical differencing of the vorticity equation, Equation 3.8, uses an Adams-Bashforth method in time and finite element method in space. These methods are respectively second and fourth-order accurate. Most of the numerical details of HOOM are discussed by Haidvogel et al. (1980). We present a schematic layout of the model in Figure 3.5.

### 3.3.3 Computational parameters

Our model configuration consists of six levels, each placed at depths corresponding to the zero crossings of the 6th baroclinic mode. In order to totally encompass the tomographic array, and minimize harmonic boundary effects, we chose to use a 1280 km square (97x97 grid) for the control ocean. And we chose the assimilation domain to be 825 km (61x61), so that the boundary



would be updated by the tomographic array.

Table 3.1 lists the numerical parameters used in the QG model. The best values for the AMODE region were used. Miller et al. (1983) discusses the vertical structure of the baroclinic version of the model, and describes the solution methods for Poisson's equation 3.9. Figure 3.5 shows the  $\psi$  modes and the depths that correspond the model's vertical levels. Figure 3.6 shows the bathymetric data used in the model simulations.

The buoyancy profile used to construct the model's vertical stratification is shown along with other hydrographic data in Figure 3.7. These profiles are spatially averaged profiles, estimated from annual Levitus data.

The integration of Equation 3.8 requires initial and boundary conditions. For these boundary conditions, we use the Charney-Fjortoft-von Neuman (CFvN) boundary conditions (Charney et al., 1950). The CFvN conditions dictate that we specify the normal velocity everywhere on the boundary and specify the potential vorticity where the normal velocity is directed inward.

Miller and Bennett (1988) demonstrated some of the difficulties that may arise near boundary points where the imposed normal velocity changes sign (the tangential flow points). Near these points, inconsistencies develop. Ultimately, these ill-posed boundary inconsistencies advect into the interior of the model and contaminate the flow field. This ill-posed nature is significant because the vorticity gradients grow in time and without bound. The incompatible boundary conditions are unavoidable in practice and will cause the model to fail on time scales comparable to those that characterize the boundary conditions. These problems highlight the definite need for data assimilation in practical ocean forecasting. New information must be introduced into the model's interior at intervals that are short compared to the forcing time scales. Whereas previous studies used four discrete waves to construct regional boundary conditions (see McWilliams and Flierl (1976)), this research uses a complete spectrum of waves.

Bottom bathymetry plays a paramount role in realistic simulation of the ocean flow field, primarily because of its influence on vortex stretching. The bottom bathymetry for the model is parameterized in terms of a nominal depth ( $H_0$ ) and a bottom perturbation,  $\hat{h}(x, y)$ , that is scaled by the Rossby number,  $\epsilon$

(not to be confused with data error). For the bottom boundary, the bathymetry,  $z$ , is given by

$$z = -H_0 + \epsilon \hat{h}(x, y) . \quad (3.17)$$

Equation 3.17 expresses the topographic variation in terms of  $\hat{h}$ , but only includes topographic variations that are consistent with the Rossby wave expansion. The bottom topography interacts with the flow field by inducing a vertical velocity,  $w$ :

$$w = \frac{D}{Dt} \sigma \psi_z = u \nabla \hat{h} = J(\psi, \hat{h}) \quad (3.18)$$

Time-stepping the bottom velocity requires the total derivative of Equation 3.18 to be re-written in terms of a partial derivative:

$$\frac{\delta d}{\delta t} (\sigma \psi_z) = J(\psi, \hat{h}) - u \nabla (\sigma \psi_z) = J(\psi, \hat{h} - \sigma \psi_{z_b}) \quad (3.19)$$

The last term in the Jacobian operation of Equation 3.19,  $\sigma \psi_{z_b}$ , is typically called “bottom density”. Equation 3.19 shows that the time evolution of the bottom density is made up of both a “topographic term” and an advection term. This advection term keeps track of bottom induced effects from previous time steps. Equation 3.19 has a form identical to that of the vorticity equation, 3.8. Numerically, the model solves for both the time evolution of vorticity and bottom density in the same way. Like the vorticity solution, the solution for the bottom density requires boundary conditions as well (they must be specified consistent with the CFvN conditions).

### 3.4 Model Interpolation and Soundspeed

Tomographic travel times measure integral properties of soundspeed anomaly ( $\delta c$ ) and current velocity,  $\mathbf{u}$ , according to Equation 2.2. This poses two problems when trying to use these travel times with numerical circulation models:

1. The tomography data does not directly measure properties of the circulation model ( $\psi, \zeta$ ), so a transformation procedure must be used to back these parameters out and also interpolate the model between the layer depths.

2. HOOM, like most other circulation models, discretely represents the vertical structure of the stream function and vorticity fields at a limited number of depths. Because the model specifies the stream function and vorticity only at a few discrete levels, interpolation methods must be used to get a smooth continuous soundspeed field. Modes or empirical orthogonal functions (which are fitted with smoothing splines) can be used to construct the interpolation functions. This method has been used by many others, but we will give a succinct review of modes; see, for example, Cornuelle (1983) as well as Gaillard (1992).

The goal of this section is to demonstrate a method for interpolating  $F(z)$  that is based on a normal mode expansion for the stream function  $\psi$ . The first interpolation method that we will discuss is based upon the so-called “dynamic modes”. The second method uses a statistical basis known as EOFs (empirical orthogonal functions). We will first discuss the formulation of the dynamic modes.

We begin by assuming that the soundspeed field,  $c(\mathbf{x}, t)$ , and density field,  $\rho(\mathbf{x}, t)$ , can be expressed as first order perturbation fields:

$$c(\mathbf{x}, t) = \delta c(\mathbf{x}, t) + c_0(z) \quad (3.20)$$

$$\rho(\mathbf{x}, t) = \delta \rho(\mathbf{x}, t) + \rho_0(z), \quad (3.21)$$

The perturbation fields,  $\delta c$ ,  $\delta \rho$ , can be further separated, not out of necessity, rather for convenience, into a vertical portion and a horizontal portion of the form  $\delta c, \delta \rho(\mathbf{x}, t) = F_h(x, y)F_z(z)$ . The vertical modes,  $F_z(z)$ , are based on solutions to Poisson’s equation 3.9 which expresses the relationship between the stream function variable  $\psi$  and vorticity  $\zeta$ . Poisson’s equation, Equation 3.9, is separable, that is  $\psi(\mathbf{x}) = F(x, y)Z(z)$ . The stream function may be written

$$\psi(\mathbf{x}, t) = \sum_{i=1}^N k_i(x, y, t)Z(z), \quad (3.22)$$

where  $N$  is less than or equal to the number of model layers. The expansion for the vorticity,  $\zeta$ , uses the same vertical basis set as does  $\psi$ . This follows from the definition  $\zeta = \nabla^2 \psi$ .

After Equation 3.22 is used in Poisson's equation (3.9), the vertical portion of the stream function equation may be written

$$\Gamma^2 \sigma \frac{\delta^2 Z}{\delta^2 z} = -\lambda Z, \quad (3.23)$$

with boundary conditions specified at the surface  $z = 0$  (although none are specified in this research) and at the nominal model bottom  $z = -H$  given by

$$\frac{\delta Z}{\delta z}(0) = \frac{\delta Z}{\delta z}(-H) = 0. \quad (3.24)$$

We numerically solve Equation 3.23 with these boundary conditions using an integrator and shooting method in order to obtain the modes  $Z(z)$ .

The soundspeed,  $\delta c$ , can be obtained using the gradient of the potential sound speed,  $C_p$ , using the following relationship:

$$\delta c = -\frac{f_0}{N^2(z)} \frac{\delta \psi}{\delta z} \frac{\delta C_p}{\delta z}. \quad (3.25)$$

Note that the gradient of the potential soundspeed is not specified by the circulation model and must be obtained from regional hydrology (see Figure 3.7). After accounting for various scaling constants used in the model and listed in Table 3.1, we can finally write the expression for the soundspeed modes in terms of the stream function modes as

$$Z(z) = \left( \frac{V_0 H}{f_0 d} \right) \Gamma^2 \sigma \frac{\delta Z}{\delta z} \frac{\delta C_p}{\delta z}.$$

### 3.4.1 Comparisons Between Statistical and Dynamic Modes

The statistical modes (typically called empirical orthogonal functions, EOFs) are based solely on statistics of the data alone. No physical model or other constraints are used. They allow a more efficient representation of the field than do dynamic modes. However, they require some type of spline interpolation between the model's layers which is required in the raypath estimation.

In order to evaluate the trade-offs between using the dynamic modes versus the statistical modes the regional climatology for the AMODE region was simulated using the QG model. In this simulation, a ten year climatological control

run was made using HOOM on a 97x97x6 model domain. The parameters and bottom topography are shown in Table 3.1 and Figure 3.6. These parameters are taken as being indicative of the AMODE region.

We then sampled this climatological simulation and estimated the amount of variance that each of the basis sets (dynamical and EOF) explained. Table 3.2 shows the percentage of the model variance explained by the dynamic and EOF modes. The first two dynamic/EOF modes accounted for 98.4%/99.2% of the overall variance. Tables 3.3 and 3.4 show these variances for each level in the QG model that is explained using the first two modes. As can be seen, both sets of modes explain the variance in the second (400 m) level the best (because the stream function and soundspeed at this depth are fairly uniform). Finally, Table 3.5 shows the coefficients of correlation between the two basis sets. As could be expected, each of the first EOF modes most closely correlates with the first dynamic mode, etc. Based on these results, we believe that the errors incurred from using a truncated set of two dynamical modes to reconstruct the QG model are negligible. And it was not necessary to use EOF modes for the purposes of this study.

Table 3.1: Computational model parameters

Symbol	Name	Value
$U_0$	velocity scale	$0.01 \text{ m s}^{-1}$
$t_0$	time scale	$1.7759010^6 \text{ sec}$
$l_0$	latitude	$25^\circ$
$f_0$	Coriolis	$6.1467310^{-5}$
$d$	x scale	$27.2155 \text{ km}$
$H$	vertical scale	$600.0 \text{ m}$
$L$	vertical scale	$27.558 \text{ (no units)}$
$\alpha$	$\beta$ Rossby number	$t_0 U_0 / d = 1.48$
$\delta t$	time step	$0.00395 \text{ days}$
$\Gamma^2$	strat. scale	$f_0^2 d^2 / N_0^2 H^2 = 0.383912$
$N_0^2$	mid-thermocline buoyancy	$2.02510^{-5} \text{ sec}^{-2}$
$N^2$	climatological buoyancy	
$\sigma(z)$	stability profile	$N_0^2 / N^2(z)$
$\psi$	stream function or pressure	
$\zeta$	dynamic vorticity	
$R$	relative vorticity	$\nabla^2 \psi$
$T$	thermal vorticity	$\Gamma^2 (\sigma \psi_z)_z$
$F$	Shapiro filter	
$K$	kinetic energy	$u^2 + v^2 / 2$
$A$	avail. pot. energy	$\Gamma^2 \sigma \psi_z^2 / 2$

Table 3.2: Percentage of the stream function variance explained by each dynamic and empirical mode.

Mode #	Dynamic	EOF
1	85.8	83.7
2	12.6	15.5
3	1.36	0.07
4	0.04	0.02
5	0.10	0.01
6	0.10	<0.01

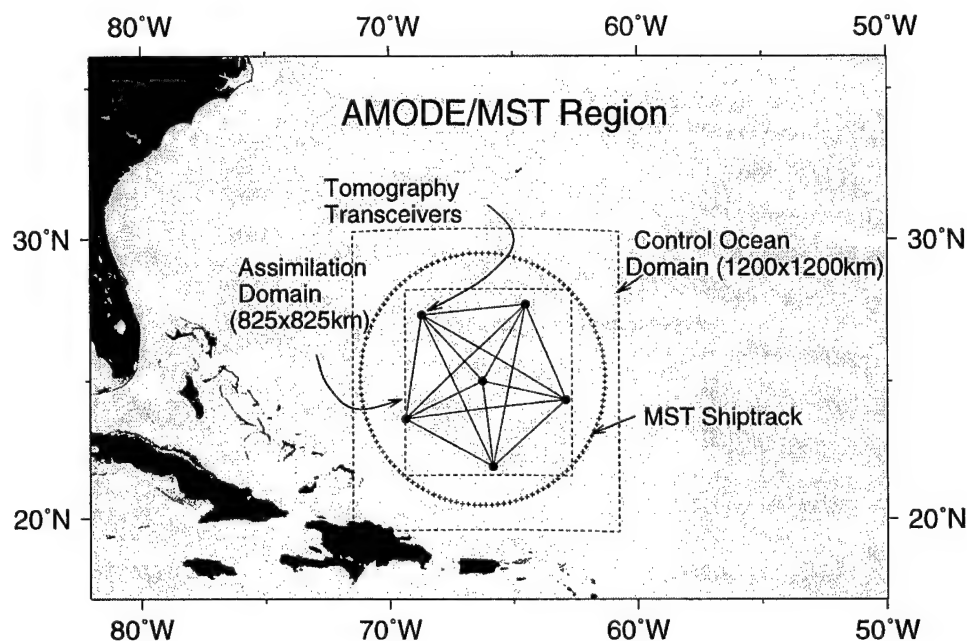


Figure 3.1: Regional map showing the AMODE region. The AMODE array is the pentagonal array; acoustic transceivers were on each mooring. The QG circulation model domain is indicated with the larger dashed box.

Table 3.3: Fraction of the variance of the stream function fields which is described by each dynamical mode according to depth.

Depth level	DM 1	DM 2	Residuals
1	59.4	37.9	2.8
2	71.3	28.0	0.7
3	90.9	6.7	2.4
4	97.4	<0.1	2.5
5	94.2	5.6	2.6
6	87.3	1.1	1.3

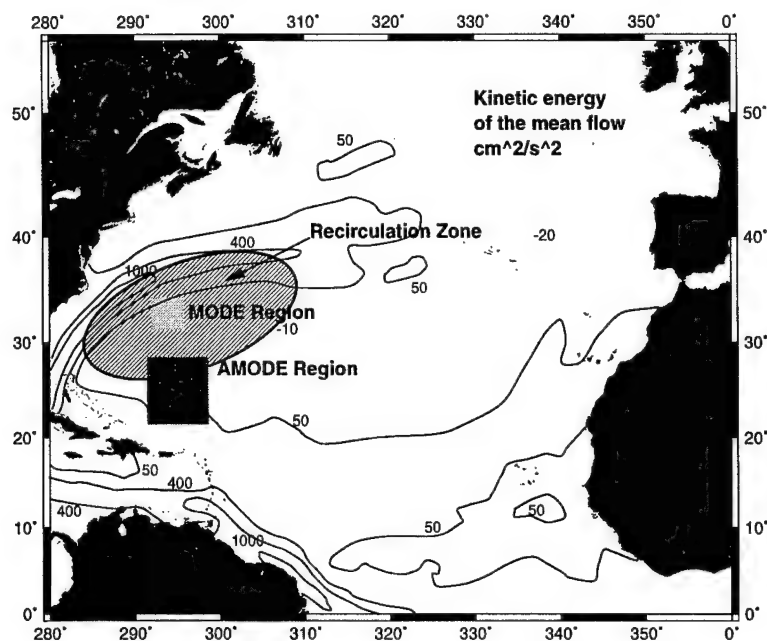


Figure 3.2: Surface eddy kinetic energy of the mean flow for the North Atlantic Region, from Wyrtekiet al. (1976).

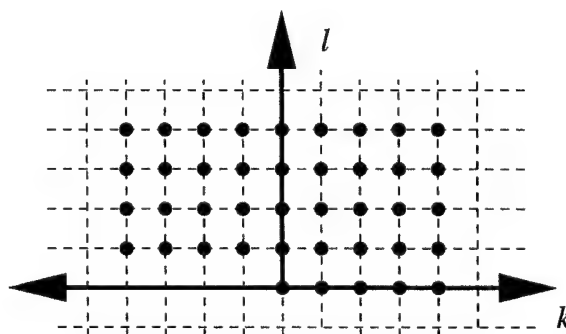


Figure 3.3: Complex wave parameters  $S_{j,l}$  which are used in the Rossby wave model. Two modes, a barotropic and first baroclinic, are used. Each mode has a set of 40 complex wave amplitudes plus the mean level, for a total of 162 model parameters (166 with the advection parameters).



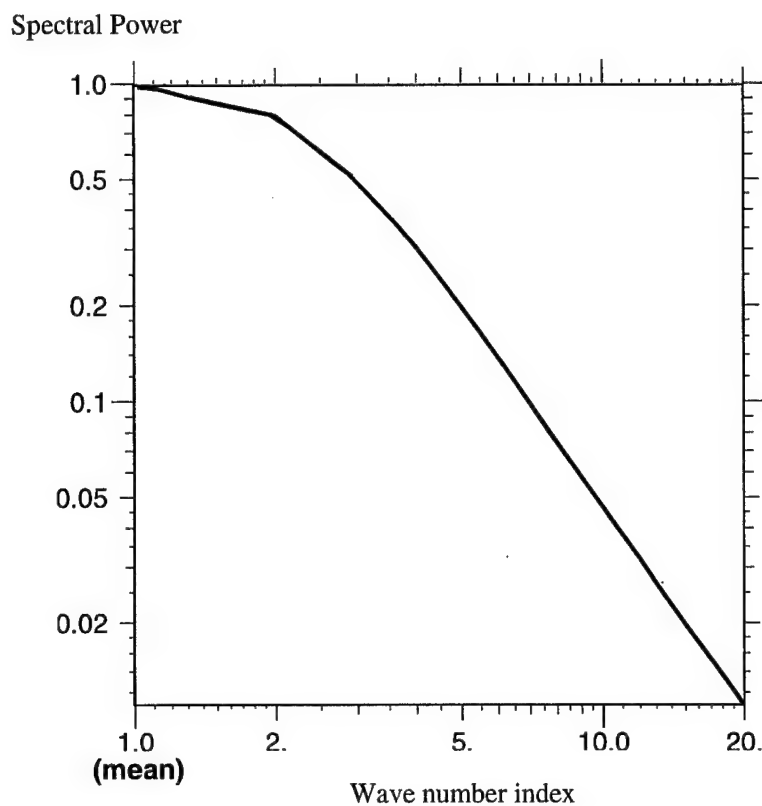


Figure 3.4: Log plot of the *a priori* model spectrum.

Table 3.4: Fraction of the variance of the stream function fields which is described by each empirical mode according to depth.

Depth level	EM 1	EM 2	Residuals
1	81.3	18.6	1.5
2	87.1	12.9	<0.01
3	95.6	2.0	2.4
4	87.6	11.4	1.0
5	80.0	19.9	1.0
6	72.4	25.6	2.0

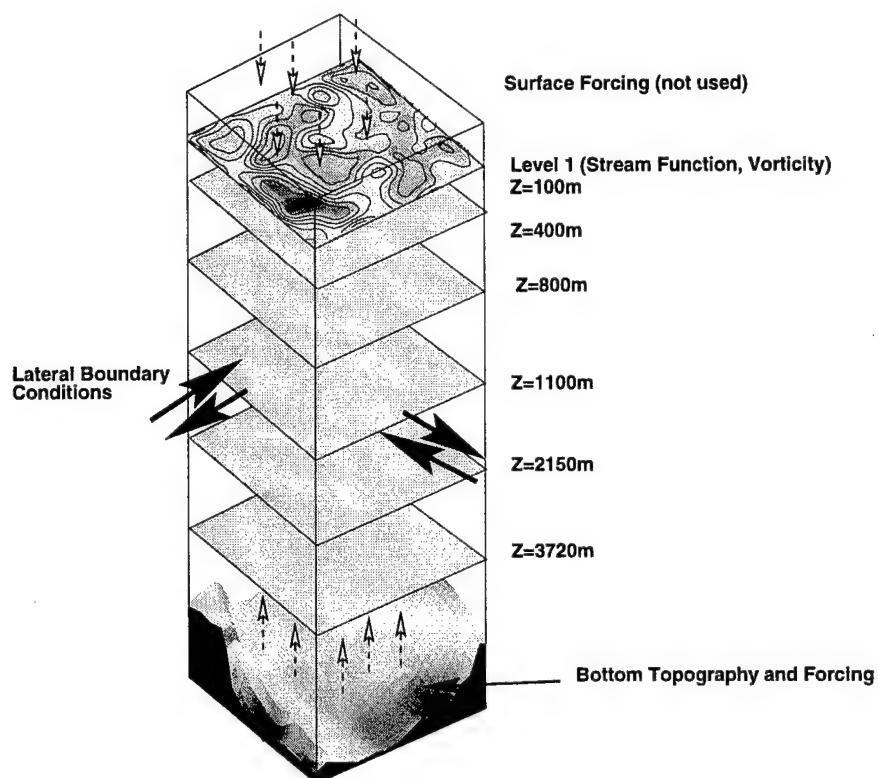


Figure 3.5: Schematic of the open ocean QG circulation model.

Table 3.5: Cross correlation energies between the empirical and the dynamical modes.

	DM 1	DM 2	DM 3	DM 4	DM 5	DM 6
EM 1	0.701	0.015	<0.001	<0.001	<0.001	<0.001
EM 2	0.269	0.773	0.050	0.002	0.004	<0.001
EM 3	0.024	0.180	0.851	<0.001	0.034	0.006
EM 4	0.001	0.010	0.035	0.947	0.059	0.012
EM 5	0.002	0.004	0.007	0.004	0.569	0.323
EM 6	0.003	0.017	0.057	0.046	0.334	0.659

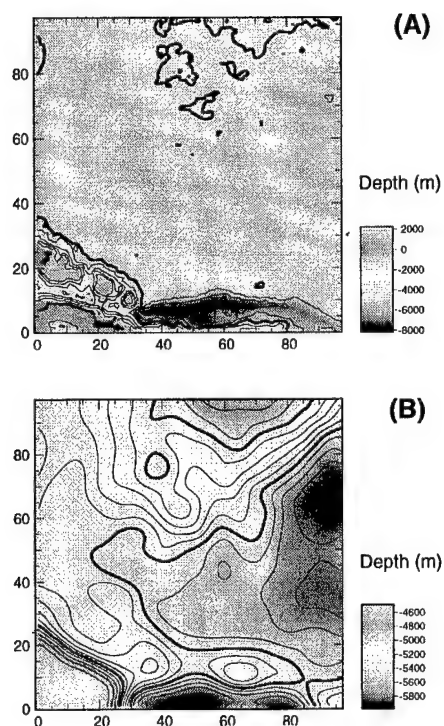


Figure 3.6: Part A shows the bathymetry based on the ETOPO5 database and resampled at the model grid interval. Part B shows a contour plot of the bathymetry data used in the QG model simulation. The data was taken from a subset of the ETOPO5 data set and filtered harmonically to be consistent with the QG dynamics.

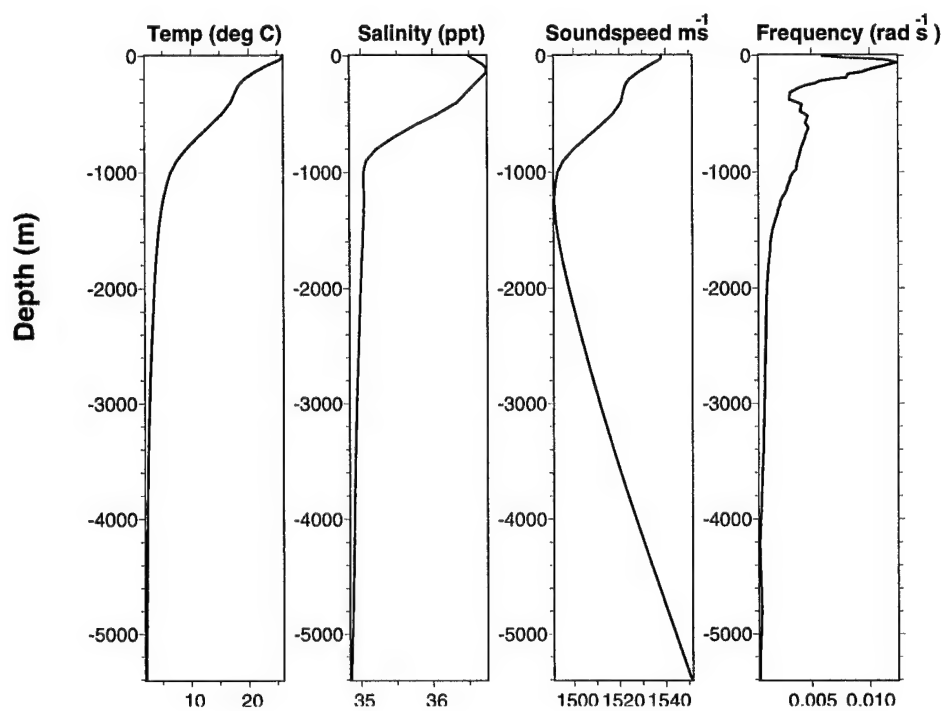


Figure 3.7: Hydrographic data used to construct the model. Plots of temperature, salinity, and soundspeed modes as a function of depth.

## Chapter 4

### RESULTS

In this chapter, we present results from three different experiments, E1, E2, and E3. In the first two experiments, we will first run a numerical twin experiment in order to validate the assimilation method and evaluate how well the measurements constrain the model.

In part, the evaluation is based on how well the measurements are able to estimate the spectrum of the barotropic and first baroclinic planetary wave field. Also, we will assess the root mean square differences of the fields, averaged over the entire model domain. The goodness of the fits is evaluated using three criteria: 1) the error weighted sum of the final residuals (an approximate  $\chi^2$  distribution), 2) the correlation coefficient,  $C$ , between the observed and predicted signal energy, and 3) the percentage of the signal variance resolved by the model,  $E$ . As used here, the  $\chi^2$  distribution should have mean one with variance equal to  $\sqrt{2/N}$  (where  $N$  is the number of observations used in the fit).

In E1 we conduct a twin experiment to show the effectiveness of assimilating point and tomographic data using the linear Rossby wave model. After presenting the results of these twin experiments, we assimilate the actual travel time data.

Next, in E2, mean large scale advection is added to the Rossby wave model. Again, a twin experiment is run, this time using simulated tomographic data. AMODE data is then assimilated and used to estimate the wave field and the large scale mean flow.

Finally, in experiment E3, we use a bootstrap approach to assimilate the AMODE data into the non-linear QG model. We call it bootstrap because we will use the Rossby wave spectrum estimated in E1 to force the boundary of the HOOM model and re-use the AMODE travel times to update the interior of the model. The assimilation method will be similar to that used in E1 and

E2, but no transition step is applied to the forecast covariance update. This form of updating is called OI (Optimal Interpolation), and is numerically much more efficient than the full Kalman update. It omits the covariance transition between assimilation time steps, which contains order  $M^2$  operations, where  $M$  is the number of model parameters.

#### 4.1 Experiment E1 - Linear Rossby Waves

In this experiment, we fit the sum and difference travel times as well as point data to a linear Rossby wave model which consists of a barotropic mode and the first baroclinic mode. A twin experiment is run, first using simulated data, then using simulated noisy data. After the results of the twin experiments are evaluated, the actual AMODE data is used to estimate the wave field.

In the twin experiments, simulated data are used to update the model at 1-day increments. We carry the assimilations out for a period of 300 days, which should allow all components of the wave field to be adequately sampled in time and space.

At each assimilation time step, the model is updated using three sum and difference travel times. The model noise,  $Q$ , is prescribed as discussed in Section 3.2. The results of the tomographic data assimilation are shown in Figure 4.1. We added random noise to the sum and reciprocal travel times. This noise corresponded to that which was typical for the AMODE data and was reduced by  $\sqrt{5}$  in order to partially account for using 3 rays per source receiver rather than 15 which were typically observed. This equivalent error level for the sum and reciprocal travel times then amounted to  $\pm 4.5$  ms and  $\pm 1.3$  ms respectively. Panel A shows the RMS error between the control ocean and the assimilation estimated at each time step (after update) in cyan. As can be seen, it slowly decreases monotonically during the run. Panel A also shows the RMS error and normalized  $\chi^2$  as a function of time.  $\chi^2$  was normalized by the number of data used in the update. In this simulation it is initially near one, but decreases slightly to about 0.7 near the end of the 300 day time period. This slight decrease is due to  $Q$  being specified slightly too large.

Also displayed in Panel A are the RMS variance in the predicted data (black) as well as the RMS of the residuals after/before the update at each time step

(blue/yellow). It is useful in evaluating the success of the assimilation process to compare the data RMS level with that of the residuals. The better the fit, the greater the reduction in variance will be.

Panel B shows the final assimilation map of the baroclinic mode at the end of the 300 day run. The maps of the eddy fields are virtually identical, with slight discrepancies near the edges of the model 122 x 122 domain, far from the tomographic array.

Panels C and D show of the error spectra as a function of time for the barotropic and baroclinic modes respectively. Keep in mind that these are error estimates for a single forecasting run. An ensemble average of numerous runs would be necessary to statistically estimate a more rigorous error field. But, this single estimate is useful for this discussion.

For comparison, Panels E and D present the analysis error estimates from the assimilation given by the diagonal elements of  $\hat{P}$ . As can be seen, certain wavenumbers are not well resolved by the array. And the errors in these particular wavenumber estimates persist in time, so that the estimate at the end of the assimilation for these waves is little better than the initial estimate.

Next, another twin experiment was performed using the linear Rossby wave model with point data. In this experiment, we will only estimate the first baroclinic mode and we will extent the assimilation period out to 600 days (in order to sample the wave field several times over). Also, we will extend the wavenumber domain out to 8 cycles per megameter from the 3.1 cycles per megameter used previously.

The point data consists of an array of 16 stations evenly spaced throughout the model domain. Each station sampled the water column at three depths in order sample the first baroclinic mode the same number of times as the tomographic data. These point measurements could be thought of as being equivalent to zero length tomographic array sampling point travel time or temperature measurements. In order to make the point and tomographic measurements as similar as possible, we will only use 3 sum travel times between each source and receiver.

A point data error equivalent to 90 ms was assigned to the point data in order for it to have an equal weighting with the tomographic measurements.

This error level resulted in both the tomographic and point data reducing the error variance at the *end* of the 600 day assimilation period to the same average or RMS level (over all wavenumbers). We will compare the two measurements by plotting the error variance in the wavenumber estimates for both data sets at a number of times during the assimilation run (see Figure 4.2). The point data's error variance is shown with dashed lines, and the tomographic data's with solid lines. As more data is assimilated, the point array's estimate of all wavenumbers decreases to its final level (marked with day 600), while for the tomographic data it decreases for the low wavenumbers only. Although both data sets reduce the average error in the wavenumber estimates to the same level, the tomographic data's final estimate for the smaller wavenumbers is better than that of the point data.

Now, we will discuss results of fitting the actual AMODE data. Figure 4.3, shows the wave parameters estimated using the real AMODE data. Like the simulations, only six travel times (3 sum/3 difference) per source/receiver pair were used in the fit. In this case the measurement error was not decreased by the  $\sqrt{5}$  factor; instead the actual measurement error of the data itself was used.

Panel A, as in the previous experiment, displays measures of how well the model is fitting the AMODE data. The  $\chi^2$  estimates of the fit are reasonable, as well as the variance of the residuals and the innovations (differences between forecast data and measured data). The high correlation coefficient,  $C = 0.84$ , and fairly large percentage of the data variance explained by the model,  $E = 60.7\%$ , indicate that the linear Rossby wave model fits the data reasonably well. Panel B shows a map of the final baroclinic stream function field. Panel C shows that the barotropic mode has some energy at higher wavenumbers. The baroclinic mode shown in Panel D has predominantly low wavenumber energies.

Although the fit to the linear model is quite reasonable, the model does not admit any large scale advection. The next section discusses results of fitting the Rossby wave field with advection.



## 4.2 Experiment E2 - Rossby Waves with Advection

In Experiment E2 we essentially repeat the previous experiments with the addition of advection to the model. The advection velocity causes Doppler shifts in the frequencies of the Rossby waves. Our model now consists of the amplitude and phases of the Rossby waves, as well as the components of the advective velocity  $U$ . Figure 4.4 shows the twin experiment results using simulated tomographic data with the travel time noise (reduced by  $\sqrt{5}$  as discussed in Section 4.1) added to the sum/difference travel time measurements.

Again, Panel A displays statistics of the data fit. The  $\chi^2$  values from the fit and the variance reductions are about the same as those of the linear Rossby waves of experiment E1. The correlation coefficient and the error variance explanation are high for the model. The true advection velocities for the twin experiment are  $u_{bc} = -0.02$  m/s,  $u_{bt} = -0.02$  m/s.

The light blue line in Panel A shows the RMS error in the estimated barotropic advection speed. It does not decrease as more travel times are assimilated, indicating that the data is not able to resolve the barotropic advection velocity. However, as shown by the light yellow line, the estimate of the barotropic advection velocity does converge to the true value. Panel B shows the final estimated baroclinic stream function map. It is very similar to that of E1. The errors in the spectral estimates of the stream function shown in Panels C and D are also similar to those found in E1.

The results of fitting the AMODE data are shown in Figure 4.5. Panel A show that the  $\chi^2$  estimates of the fit are reasonably close to unity as in Experiment E1, and that the variance reductions are fairly good.

Panels C and D also show that the estimated spectrum of Rossby waves is nearly identical to that of the non-advective model. Panel B shows the estimated advection velocities for both modes. The estimates for the advection of both modes are not statistically different from zero.

The correlation of the fit and the variance reduction (0.85/62.15%) are virtually identical to the linear Rossby wave fit. Given that the twin simulations indicated that the tomographic data were able to resolve the baroclinic advection rates, it is reasonable to suggest that baroclinic advection is not a significant factor in the AMODE region.

### 4.3 Experiment E3 - Non-linear HOOM model

In Experiment E3, the travel time data were assimilated into the non-linear QG model. The necessary boundary conditions for the circulation model were supplied using the Rossby wave field estimated with the Kalman filter in Experiment E1. The boundary conditions were applied to all six levels of the model at an update rate of once per day.

Before assimilating data into the interior of the model, we conducted a simple predictability experiment. Travel time data was withheld from the interior, and only the boundary of the model was updated. Here, we wished to demonstrate how long a time period the model was able to continue to predict the interior travel time data. Further, we wished to estimate how often interior data needed to be assimilated into the model. To evaluate at what point the model diverges from the measurements, we compared the differences between data that the boundary driven model predicts and the AMODE data. Panel A in Figure 4.6 shows the RMS level of these residuals and the RMS level of the AMODE travel times. After a period of about 60 days, the predicted data has diverged from the measurements. This is an indication that the QG model requires interior updating within at least the 60 day time frame in order to maintain any degree of predictability. The wavenumber spectra of the model are shown in Panels C and D of Figure 4.6. They show the energy to be predominantly low wavenumber, with the barotropic mode having somewhat more temporal variability.

Results of the interior assimilation are shown in Figure 4.7. The  $\chi^2$  of the fit grows a bit during the 220 day assimilation period, but remains within reason. The RMS of the innovations consistently remains lower than the RMS of the data. Panel B shows the final baroclinic assimilation map for year day 350.

Panels C and D show the wavenumber spectra for the model. The wavenumber spectra of both modes are red. Comparing with Figures 4.3 and 4.5, the wavenumber estimates are slightly different than those estimated using the Rossby wave models which tended to have more energy in higher wavenumber components.

Plots of the time evolution of the stream function and vorticity RMS energies and the kinetic energies are shown in Figure 4.8. All of the energy levels

are initially low, and begin to increase after year day 180. This general increase in energy also matches an increase in the baroclinic energy estimated in E1 using the Rossby wave model.

Panel A shows the stream function RMS energy as a function of time for each of the six levels in the QG model ("1" being shallowest to "6" the deepest). The upper two levels contain most of the energy, roughly twice that of the lower 4 levels. Panel B shows the RMS energies of the stream function in terms of modes. Nearly all of the variability is contained in the first two modes. Some energy is being transferred to higher modes by the model, as can be seen by the increase in the energy for the third mode. This transfer of energy is a non-linear process, and arises from mode-mode interactions within the QG model. Panels C and D show level/mode time histories for the vorticity. They show a similar story as the stream function: most of the energy is contained in the upper levels and first two modes, but a bit more energy appears to be imparted to the higher vorticity modes (Panel D). The upper panel shows the RMS kinetic energy in terms of both level and modes. The upper level kinetic energies appear to be between 20–30 ( $\text{cm}^2 \text{s}^{-2}$ ), and the kinetic energy is roughly equally partitioned between the first two modes.

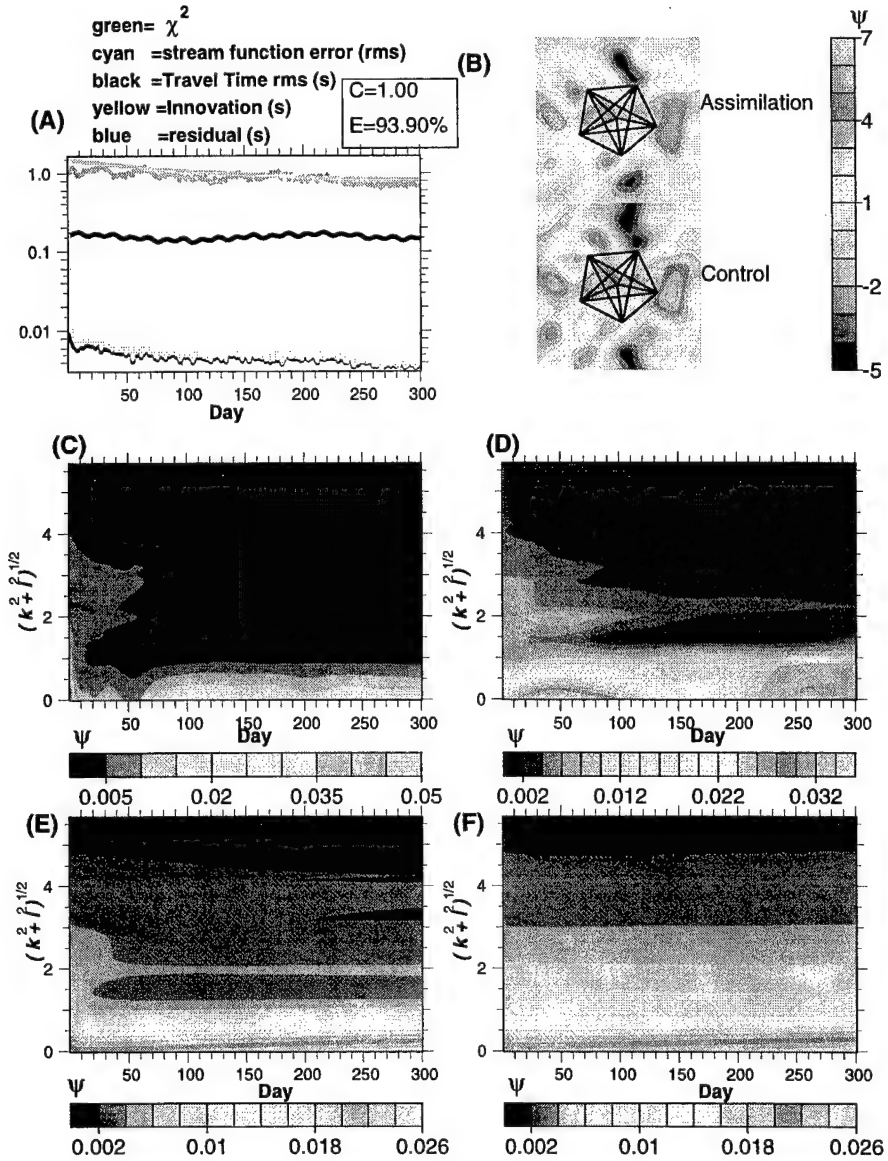


Figure 4.1: Panel A) RMS error levels. Panel B) Final assimilation and true (control) field estimates for the baroclinic mode. Panel C) Differences between the estimate and control ocean for the barotropic mode in terms of the wavenumber space ( $CpMm$ ). D) Differences between the estimate and control ocean for the baroclinic mode in terms of the wavenumber space. Panel E) Estimated spectral errors in the barotropic mode. Panel F) Estimated spectral errors in the baroclinic mode.

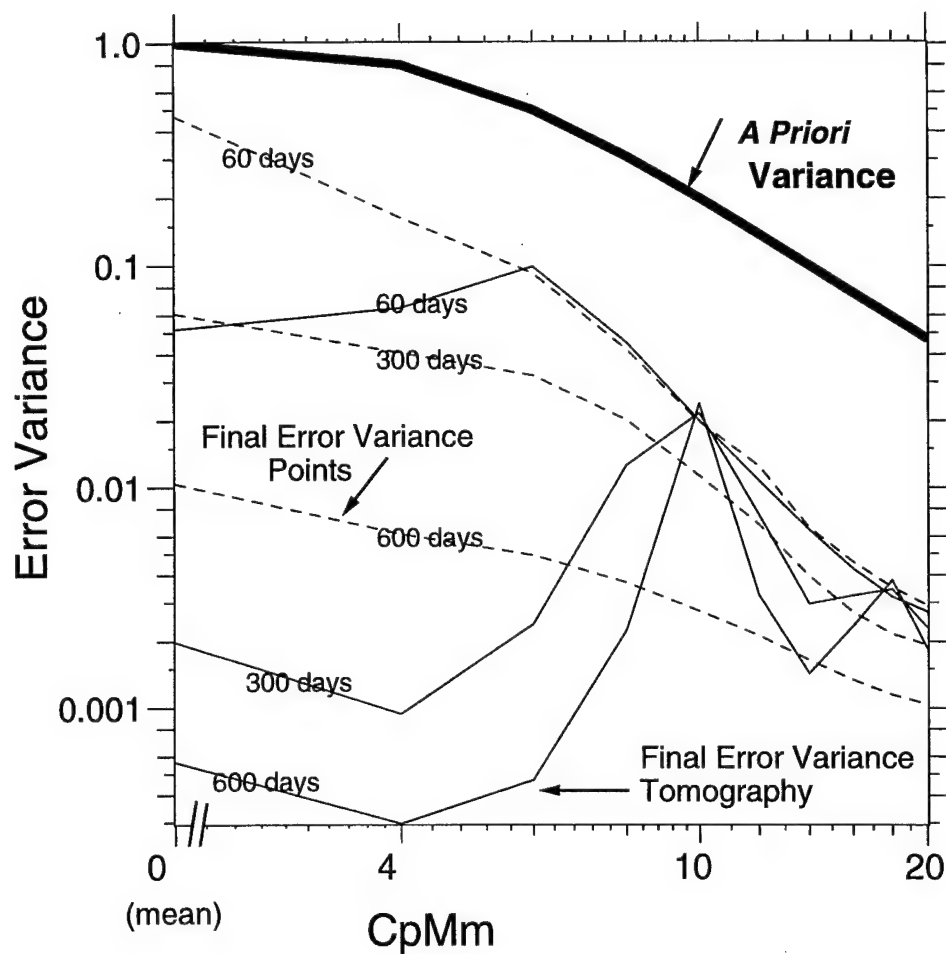


Figure 4.2: Comparison between error in the wavenumber estimate as a function of time for the point measurements (dashed lines) and the tomographic measurements (solid lines). This figure shows the error reduction in wavenumber space at 3 different times during the assimilation of the point and tomographic data.

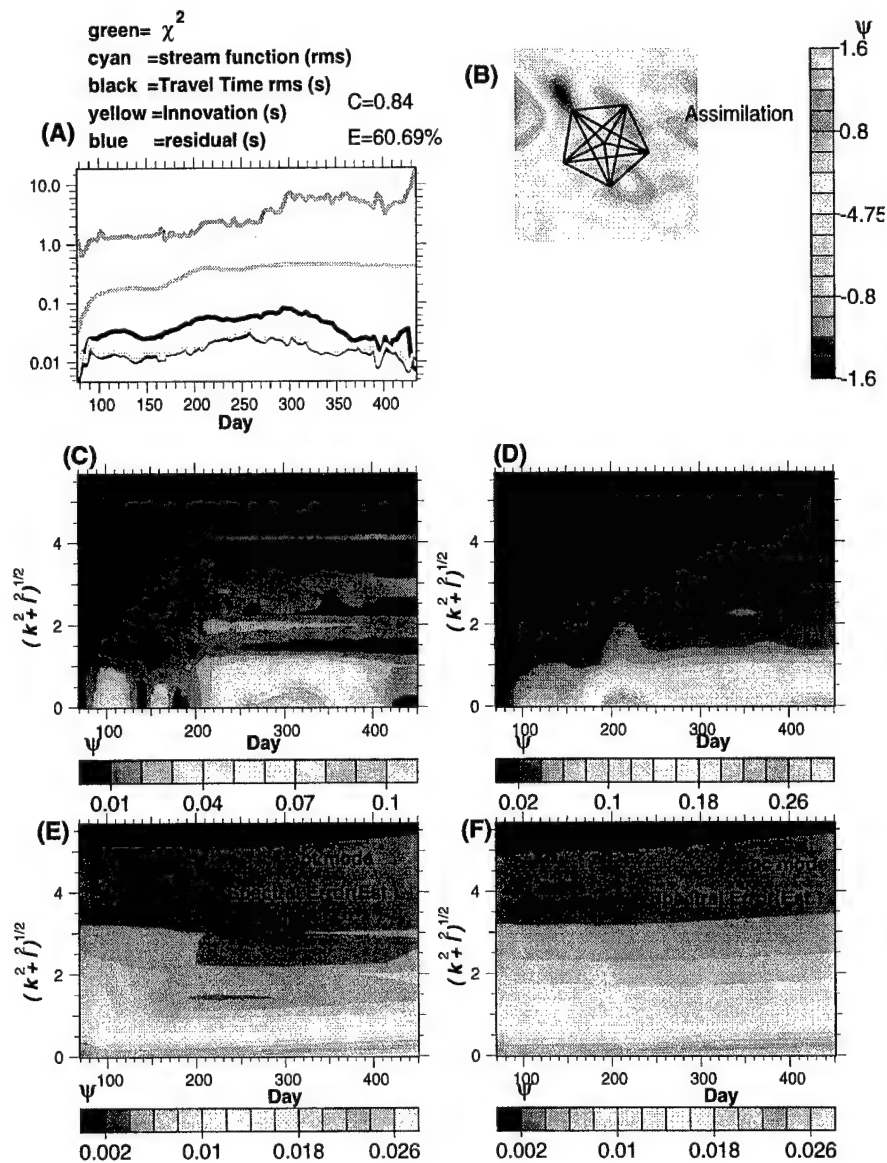


Figure 4.3: Panel A ) RMS error levels. Dark yellow/blue are the residuals of the forecast/analysis. Panel B) Final assimilation for the baroclinic mode. Panel C) Barotropic mode amplitude in wavenumber space (CpMm). D) Baroclinic mode amplitude in wavenumber space. Panel E) Estimated spectral errors in the barotropic mode. Panel F) Estimated spectral errors in the baroclinic mode.

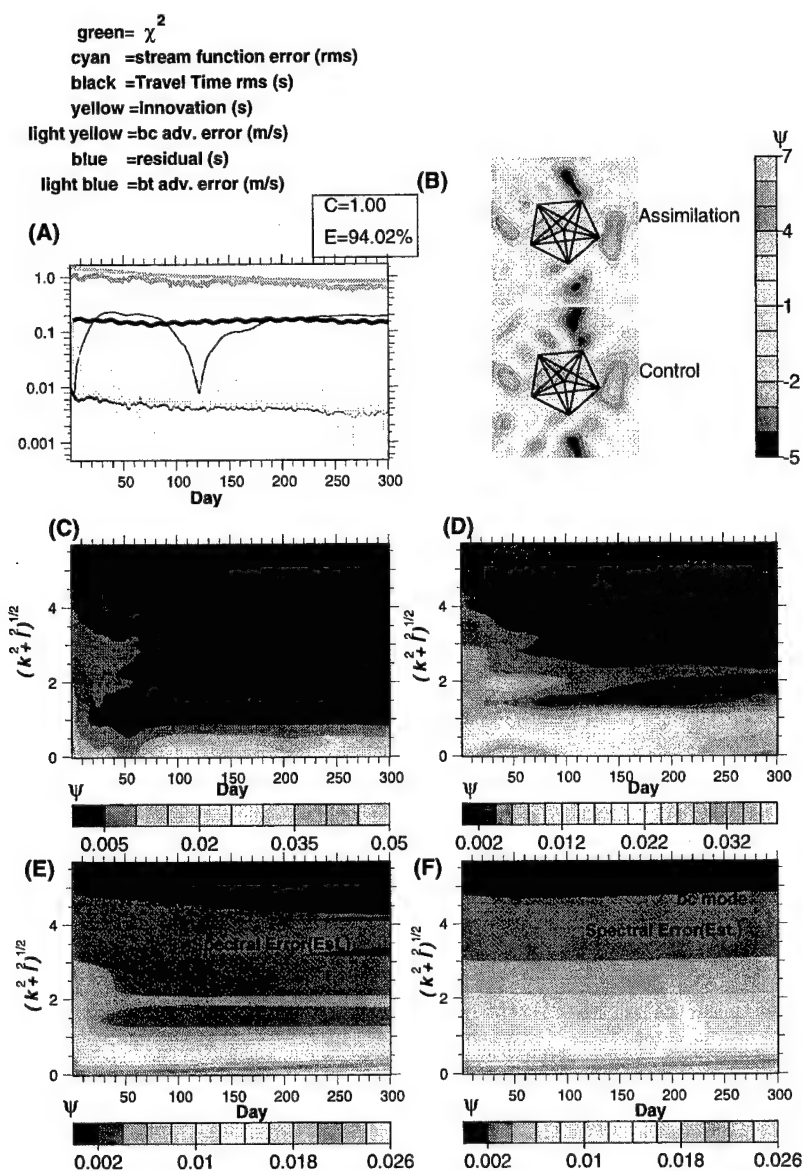


Figure 4.4: Panel A) RMS error levels. Dark yellow/blue are the residuals of the forecast/analysis, light yellow/blue are the errors of the magnitudes of the bc/bt velocity estimate. Panel B) Final assimilation estimates for the baroclinic mode in physical space. Panel C) Differences between the estimate and control ocean for the barotropic mode in terms of the wavenumber space (CpMm). D) Differences between the estimate and control ocean for the baroclinic mode in terms of the wavenumber space. Panel E) Estimated spectral errors in the barotropic mode. Panel F) Estimated spectral errors in the baroclinic mode.

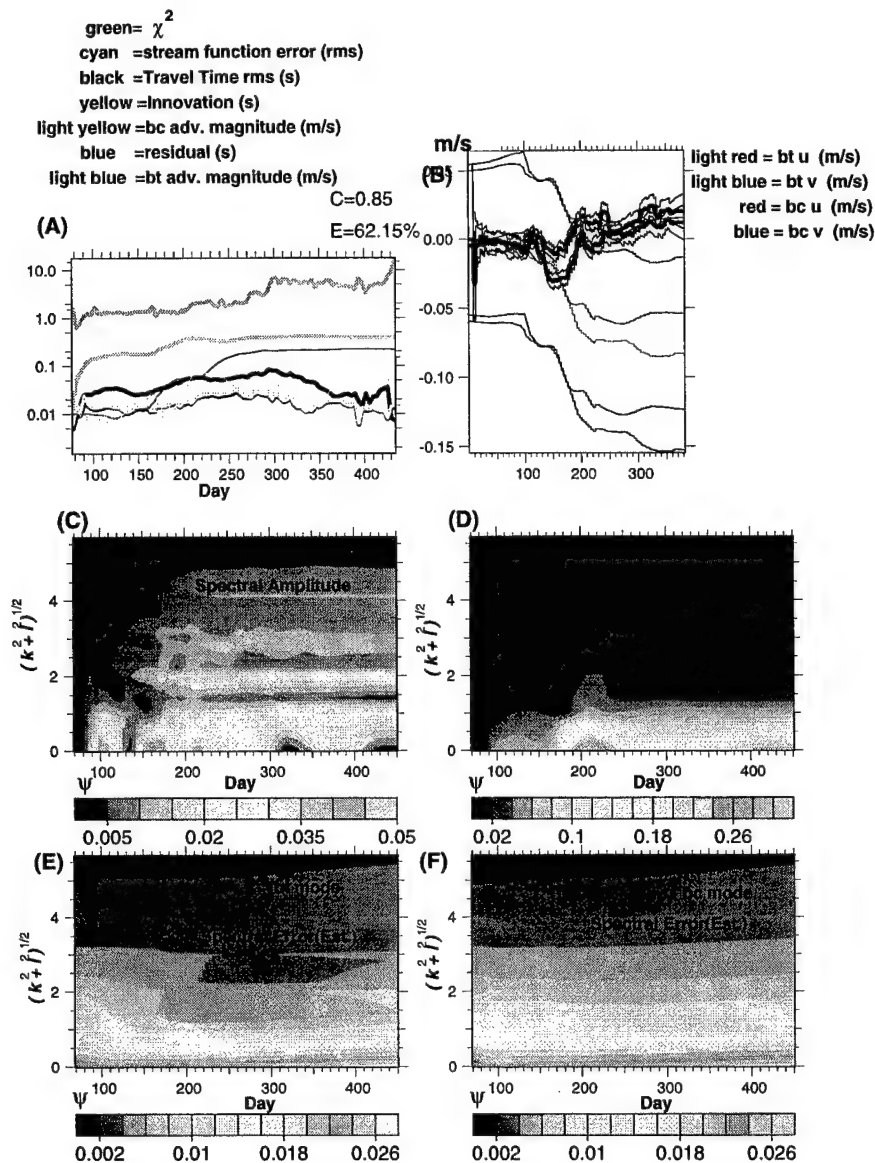


Figure 4.5: Panel A) RMS error levels.

Dark yellow/blue are the residuals of the forecast/analysis, light yellow/blue are the errors of the magnitudes of the bc/bt velocity estimate. Panel B) Estimated advection velocities and error bars (shaded). Panel C) Differences between the estimate and control ocean for the barotropic mode in terms of the wavenumber space (CpMm). Panel C) Barotropic mode amplitude in wavenumber space. D) Baroclinic mode amplitude in wavenumber space. Panel E) Estimated spectral errors in the barotropic mode. Panel F) Estimated spectral errors in the baroclinic mode.



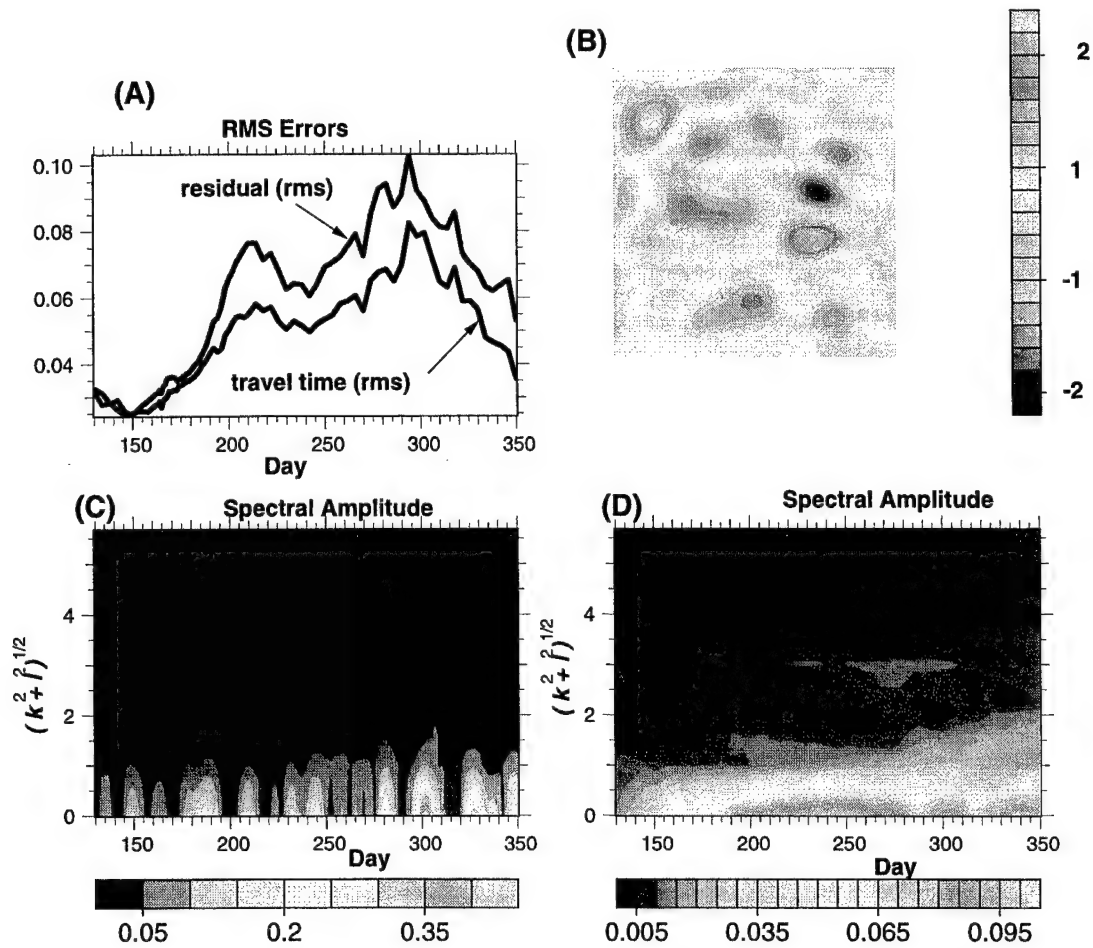


Figure 4.6: Panel A) RMS of the measured data and the difference with data predicted by the boundary force HOOM model. Panel B) Final field in physical space. Panel C) Amplitude of the barotropic mode in spectral domain (CpMm). Panel D) Amplitude of the baroclinic mode in spectral domain.

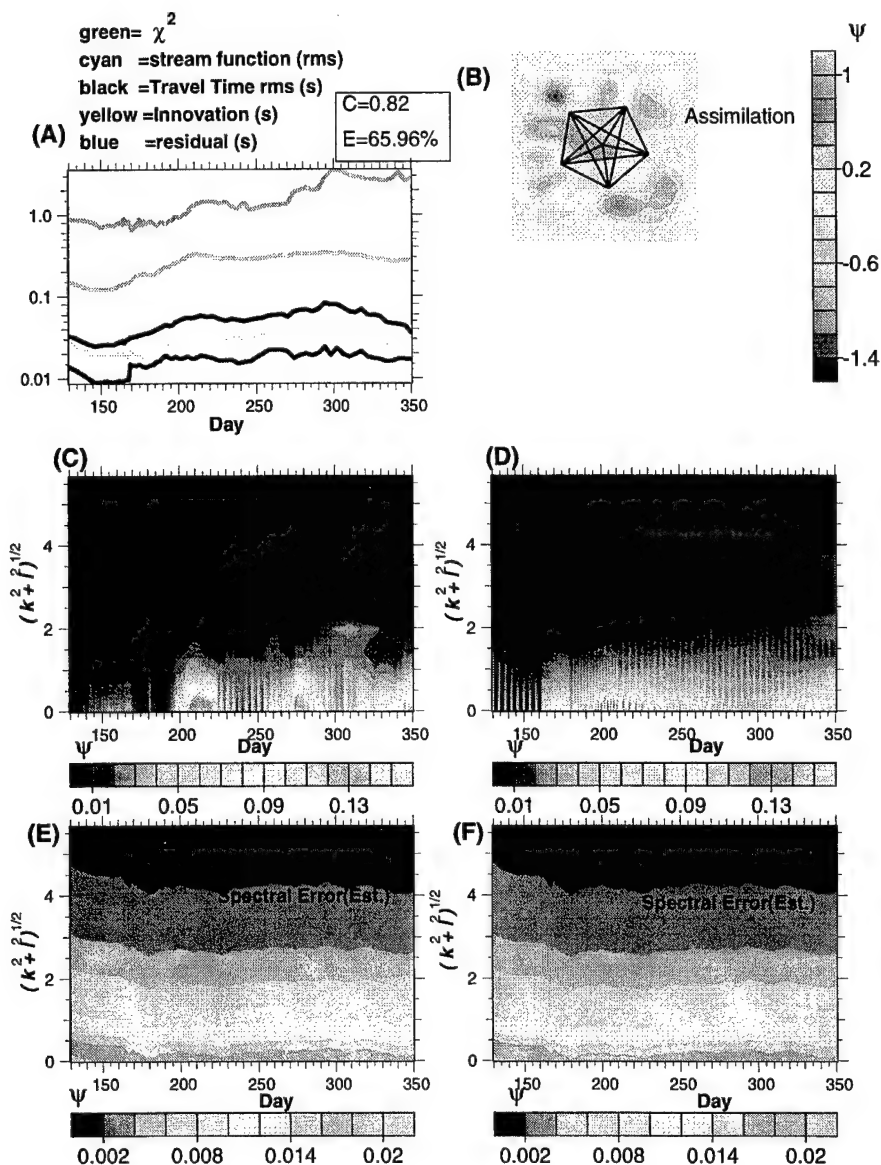


Figure 4.7: Panel A) RMS errors. Panel B) final analysis field. Panel C) Barotropic mode amplitude in wavenumber space. D) Baroclinic mode amplitude in wavenumber space (CpMm). Panel E) Estimated spectral errors in the barotropic mode. Panel F) Estimated spectral errors in the baroclinic mode.

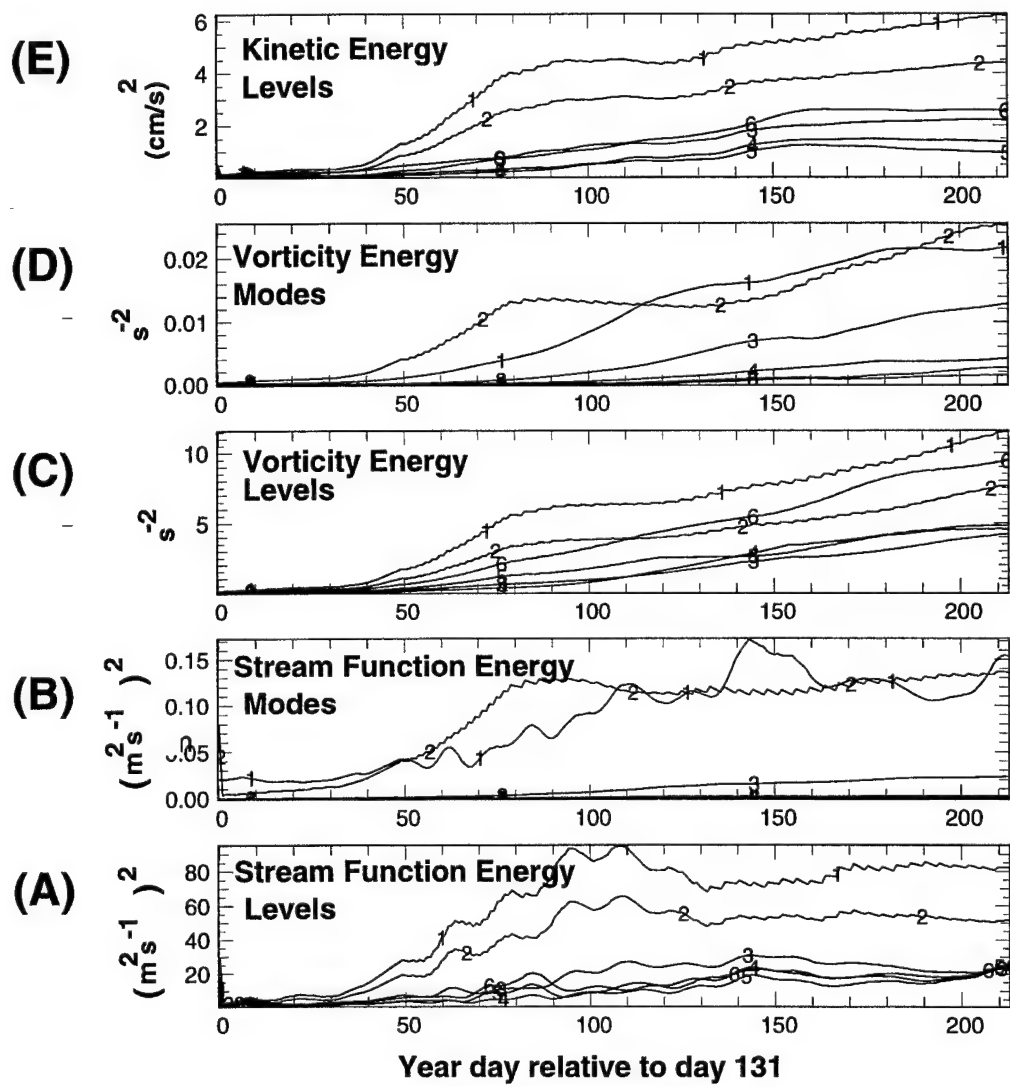


Figure 4.8: Quasi-geostrophic energies. (See text for description.)

## Chapter 5

### DISCUSSION

We began with the hypothesis that acoustic tomographic measurements are uniquely important because they are sensitive to low wavenumber properties of the ocean, and that the inherent integrating nature of the measurements must be accounted for when the data are assimilated into numerical ocean models.

Munk and Wunsch (1979) first introduced the concept of ocean tomography as a means of determining the eddy-scale structure of the ocean. They showed that acoustic travel times could be used to measure integral or average properties of soundspeed (which to first order is linearly related to temperature) and current velocity along raypaths between an array of sources and receivers. Further, they showed to first order that the one-way travel times could be related to the integrated temperature anomaly along the ray, and that the differenced travel times could be related to the integrated current velocity along the ray.

By using an array of acoustical transceivers these temperature and current fields can be mapped over a region of the ocean. Although the "times of flight" of the acoustical signals between transceivers are nearly instantaneous, typical tomographic experiments are designed to repeatedly sample the ocean and generate long time series of measurements over several weeks or months. During these time periods the ocean fields may appreciably change and the latency or time dependence of the data must be taken into account.

Over the last two decades, a growing number of tomographic experiments have been conducted in many of the world's oceans. One such experiment, AMODE, was located north of Puerto Rico. During this experiment, an extraordinarily long time series (220 days) of tomographic data was collected. These data were specifically designed to resolve the eddy scale temperature and current variability.

In part, this research was motivated by the availability and need to analyze a data set such as the AMODE data, as well as by a series of workshops

sponsored by ONR. The primary goal of these workshops was to foster communication between the ocean modeling community and the data acquisition community. Naturally, integral measurements such as tomography are only one piece of a total ocean observing system. These workshops discussed how to incorporate many different forms of data into time-dependent ocean models including point or localized measurements.

### **5.1 Parameterization**

In order to explain why we parameterized our model the way we did, we need to step back and look at the fundamental properties of the tomography data which measure integral properties along acoustical ray paths. First, we considered a set of raypaths along any given vertical slice between a source and receiver. These raypaths are determined by the soundspeed structure in the ocean which acts as a dispersive wave guide. For purposes of this research we characterized these raypaths using an average or background soundspeed field and we estimated perturbations to this reference. For typical soundspeed anomalies associated with the eddy fields in the AMODE region, the acoustical paths were assumed fixed, i.e., their locations were unperturbed by the soundspeed anomaly. This assumption was tested by calculating ray trajectories through perturbations that were reasonable for this region. This assumption was found to be valid.

Because these rays spend most of the time near their turning depths, they are particularly sensitive to temperature and current anomalies at those depths. The raypaths are controlled by the dispersive wave-guide properties of the ocean propagation. Only a limited number are typically discernible between the source and receiver (15–20 for the AMODE experiment). Hence along any vertical tomographic slice, the rays will only sample a limited number of depths and produce rather coarse vertical resolution. In the horizontal plane, resolution is determined by the number of crossing paths between the sources and receivers. Theoretically, we could have an unlimited number of them, but because of limited budgets, we must make do with as few as possible.

Given these limitations of the tomographic vertical and horizontal sampling

properties, some method had to be developed to parameterize soundspeed and current fields in the horizontal and vertical directions. The parameterization had to serve three purposes: 1) reduce the number of model parameters which we needed to fit the travel time data, 2) provide a means of interpolation, and 3) provide a means of converting between soundspeed and current parameterization and the parameterization used by the circulation models (stream function and vorticity which will be discussed shortly).

There are several possible basis sets which could be used. For instance, triangle or Gaussian shaped functions (these were used early on in this research, but discarded for reasons stated below) or functions that are based on the statistical soundspeed/current variability of the circulation model or the ocean itself (EOF's). Because EOFs are eigenvectors of the fields covariance matrix, they provide the most efficient representation of the field with the fewest modes. Unfortunately, EOF's do not have continuous derivatives which is a necessary condition to produce realistic soundspeed modes. In other words, rays could not be re-traced through the soundspeed field. In this research, we ultimately chose a parameterization related to the physics of the problem.

In the vertical, we chose to use dynamical modes. These modes are based on QG theory, and only the first two modes are necessary to explain 98% of the variance in the temperature and current fields of the AMODE region. Not only are they related to the physics of the flow, but they are an efficient basis set as well. Also, these modes can be conveniently related to the soundspeed modes using buoyancy frequency and the gradient of potential temperature.

With the barotropic mode having no zero crossings, the first baroclinic mode has a crossing at a depth of about 1400 m in the AMODE region. The barotropic mode is constant in depth and has no temperature or soundspeed mode signature, but it does have a significant current velocity signature. This mode was used to describe the vertically uniform current field. Theoretically, in the absence of bottom topography, its radius, or length scale of deformation, is infinite.

The first baroclinic mode has a single zero crossing and a maximum at the surface. Its equivalent soundspeed mode has a maximum at a depth of about 700 m and a theoretical deformation radius of about 50 km. Each successive

mode will have an additional zero crossing and a shorter deformation radius.

In the horizontal, we chose to use sines and cosines. This choice was based on two main factors. First, we wished to estimate the spectrum of Rossby waves. Secondly, based on our hypothesis, we wished to evaluate the performance of the data assimilation experiments in terms of the wavenumber domain. We previously mentioned that each vertical dynamical mode has a corresponding radius of deformation; it is important to keep in mind that the model wavenumber domain should be made large enough to resolve the particular mode of interest. If higher modes are used, more wavenumbers should be included in the wave field in order to resolve the higher order modes.

A drawback to using sines and cosines is that they do a very poor job of extrapolation away from the data domain. Also, they can force periodic boundary conditions on the solution if the physical domain boundaries are not at least 1.5–2 times larger than the data domain. In this research, we strived to eliminate this effect by choosing the appropriate model domains.

We do in effect extrapolate the Rossby wave field in order to produce boundary conditions for the QG model; however, we try to minimize the extrapolation errors on the interior domain of the model by choosing the QG domain to be sufficiently large so that the assimilation of interior data can correct this.

## **5.2 *Twin Experiments***

We made use of several twin experiments. The utility of the twin experiment was to demonstrate the effectiveness of a particular data set or combination of data sets when they are assimilated or combined with an ocean circulation model. The main purpose of the twin experiments was to make comparisons between a control model and another model which is being updated or corrected using synthetic data derived from the control ocean. Data assimilation was used to make the corrections to the twin model's parameters. The twin model was advanced in time using the same physics as the control model (this does not imply that the model was noise free because the interior and boundary are not exact). Hypothetically, if the data were perfect (noise free and able to resolve all scales of the model), the model noise estimates were perfect, and an assimilation method that fully propagated the estimates and their errors were

used, results of the two models should converge. To the degree that any of these things is less than perfect, the assimilation and the truth will not converge.

Typically, there is little point in conducting a twin experiment that uses perfect data, so we sampled the control model and contaminated the synthetic observations with noise commensurate with some *a priori* noise assumptions ( $R$ ). The twin experiment was used to determine how to adjust  $Q$  (the model forecast covariance) so that the estimate and the control oceans converge optimally. In as much as we have confidence that this twin experiment represented nature, we used these estimates for  $Q$  to guide us when assimilating real data.

Although we learned a great deal from the twin experiments, for example, sensitivity of the estimate to  $Q$ , there are several things we could not learn. For example, they cannot tell us if our measurement model,  $h(x)$ , is correctly modeling our observations. The measurements will always be self consistent with the model. The normalized  $\chi^2$  estimate (the distribution of the residuals weighted by their errors) from the fit will be sensitive to changes in  $Q$ , but not to changes in the data error, since the noise added to the data is statistically consistent with the *a priori* data error. This means that in order to validate the measurement model, separate comparisons need to be made between modeled data and actual data.

### 5.3 Assimilation Techniques

Data assimilation is a term used for various techniques of incorporating or combining data into a time dependent model. Intrinsically, all of the assimilation methods can be considered simplifications or recursive estimates of the more general least squares estimate of the model state over all space and time. Except for all but the simplest linear models (even with the parameterization mentioned previously), this quickly becomes computationally infeasible. Therefore sequential methods, such as the Kalman filter, are used to estimate the model state and its errors at successive time steps during the evolution of the model.

The Kalman filter requires in its transition step the computation of the mode error covariance, which is very computationally intensive. For linear models (the Rossby wave models), the transition matrix can be thought of as



a tri-diagonal matrix which phase shifts the wavenumber components of the model. The full Kalman filter was used for the Rossby wave models.

However, for the QG model, there is no simple expression for the transition matrix. The transition matrix is dependent upon the current estimate of the stream function and vorticity fields. For this model, optimal interpolation (OI) was used, wherein the model was used to forecast the state at the appropriate time step, but not its error covariance. This can be viewed as using  $I$ , the identity matrix, in place of the transition matrix for the calculation of the forecast model error covariance. Although advection of information is lost in such a covariance update, information about correlations in the data is retained (from the analysis step  $P_a = (I - KH)P_f$ ).

A number of twin experiments were conducted using the linear Rossby wave model in order to evaluate the penalty associated with this sub-optimal transition step. After tomographic data was assimilated over several realizations of the wave field, the RMS error in the Kalman filter estimate was 10%, and the RMS error in the OI estimate was 18%. The difference between the two eventually became negligible after assimilating more data.

#### 5.4 Errors

The twin experiments used theoretical travel times contaminated with random errors whose variances were simply specified as constants for the sum travel times and the difference travel times. These constants were based on average error estimates obtained from experience with the AMODE data. The constant used for the reciprocal travel times,  $\sigma = \pm 3$  ms, was larger than that normally observed for experiments such as this (Dushaw et al., 1996). It is believed that these errors may be reduced by improved mooring tracking analysis of the AMODE data (B. Dushaw, personal communication, May 1999).

The error estimates contained the accumulative effects of: 1) residual mooring motion (sum travel times only), 2) uncorrected clock drift, and 3) internal wave noise. Additional errors from assuming that the raypaths were unperturbed are on the order 0.1 ms and were not included in the error budget. In hindsight this error source should have been added for completeness. In the twin simulations, the travel time errors were artificially lowered (by dividing

the error by  $\sqrt{5}$ ) in an effort to simulate the use of 15 ray arrivals while using only 3. This was valid given that we were only using two vertical modes, which were adequately constrained (the eigenvalue spectrum only contains 2 significant eigenvalues). Therefore, if the experiments were repeated using all 15 available rays, the results should not be significantly different.

### 5.5 Models and Results

We chose to assimilate the tomographic data using three different models. The two Rossby wave models were specifically chosen for their simple dynamics. These simple dynamics allowed the Kalman filter to be used for the updating. We did not expect them to realistically describe the flow in the AMODE region. The QG model was chosen because it was a non-linear extension of the linear Rossby wave models (the Jacobian and bottom topography set them apart) and provided a more realistic situation.

The results of the twin experiments with the linear Rossby models showed that the tomographic data (E1) resolved the low wavenumber components of the Rossby wave field. The RMS difference between the final assimilation estimate of the Rossby wave field and the control ocean at the end of the assimilation period was decreased by about 50% from its starting value. We explored using various estimates for  $Q$ . These included using an adaptive  $Q$ , and  $Q = 0$  at all. Although  $\chi^2$  was sensitive to these changes, the final RMS difference was not. Maps of the difference between the fields did show some minor improvements when  $Q = 0$ . This is expected because with non-zero  $Q$  we effectively over-weighted the observations and under-weighted the model.

Point data were also assimilated into the linear Rossby wave model. The number of measurements was approximately equal to the number of sum travel times. The data error for the point measurements was adjusted so that the average error in the final wavenumber estimates at the end of the assimilation period was comparable to that produced by the tomographic assimilation. Although the error wavenumber spectra estimates for both data were initially similar, at the end of the 300 day period the tomographic errors for the low wavenumber components were less than those for the point measurements. This finding was consistent with the integral nature of the tomographic mea-

surements. The noise level of the point measurements was effectively  $\pm 90$  ms, about 20 times larger than the travel time errors.

Results of the twin experiment that included advection were nearly identical to the non-advection experiment. The RMS reduction in the difference between the estimated and true stream function fields decreased by 50%. The barotropic advection components, which are determined by the difference travel times, could not be resolved. Most likely this is because the very small travel time signature of this barotropic advective component ( $\approx 0.8$  ms) was swamped by the difference travel time noise.

### 5.6 Real Data

Both of the Rossby wave models fit the actual AMODE travel time data in a manner consistent with the assumed error levels in the data and *a priori* model errors. The correlation coefficient between the measured data and that predicted by the models was 0.84, and the variance reduction was 61% for both models, indicating that both models on average fit the data equally as well.

The normalized  $\chi^2$  estimates from both model fits were nearly identical, and remained near 1 until year day 300, when they increased. This corresponds to the time at which most of the transceivers failed and there was only data from 2 or 3 moorings. Since the wavefields estimated by both models were nearly identical, we describe next the wavenumber fit from the non-advective model.

The spectra of both modes had roughly the same shape. This is not unexpected, since the same *a priori* spectrum was assumed for both modes. In hindsight, this was not wise. The barotropic spectrum should have been redder (based on the internal deformation radii).

Some of the details of the time evolution of the mode spectra are quite interesting. For instance, there were several episodic rises and declines in the strengths of the two modes. These rises and declines did not occur at the same time for both modes. It is suggested that these packets of activity represent periods of more intense wave activity. For the barotropic waves, there were two brief increases near year days 100 and 160, and then a longer duration increase between year days 250 and 350. For the baroclinic mode, there was a 60 day intensification starting near year day 180 which was followed by a slight

decrease in amplitude.

The fits to the QG model reduced somewhat more of the travel time variance (66%) than the Rossby wave models (61%). The  $\chi^2$  of the fit was similar to the Rossby wave fits, with a similar increase after day 300. The RMS level of the forecast residuals was greater than for the Rossby wave model. We feel we could improve this with better estimates of  $Q$ .

The time evolution of the mode spectrums was a bit different from the Rossby wave fits. The barotropic mode showed an increase in amplitude near year day 200, about 50 days earlier. Also this intense period only lasted about 50 days. Another intense period occurred near year day 280 and died off by day 300. The evolution of the baroclinic mode spectra shows no major difference with the Rossby wave evolution. However, examination of the physical space maps of the two did reveal subtle differences in the amplitude and phase of the stream function fields.

The spectrum of the baroclinic mode for the QG models, on average, has slightly more high wavenumber energy than the spectra of the linear models. This higher wavenumber energy is a result of the model's interaction with topography. More energy in these higher wavenumbers may account for the increased variance reduction in the QG model's fit.

Regional models, such as HOOM (HOOM is the Harvard Open Ocean QG model used in this research), require boundary conditions, and some means of extrapolation must be used if the interior data is insufficient (in time or space) to supply those conditions (Bennett, 1992). There are a number of possible alternatives besides the method that was used here (Kalman filtered estimates of Rossby waves), such as extrapolation from the interior data or large-scale forcing from global circulation models. This is conceptually attractive, but as data is assimilated into the the model's interior, serious discontinuities could develop near the boundary region. Secondly, the boundaries could have been expanded outward several hundred kilometers from the assimilation region. This is numerically unattractive because it requires extra computation time. A third possibility for supplying boundary conditions would be to use data from the interior in conjunction with some form of objective mapping. This was attempted early in this research but found to be problematic because of sudden

temporal jumps in the boundary, which the circulation model did not have time to adjust for. These jumps resulted in spurious growth in the stream function and vorticity fields.

The approach to boundary conditions used in the QG model experiment attempted to make use of the interior data and still prescribe the boundary conditions in a manner consistent with the model dynamics and the interior data. In this research, we re-fitted the interior data once; this process could be further improved with more iterations. That is, after the first iteration, we could have refined the boundary conditions and re-assimilated the interior data a second time.

Experiment E3 indicated that the QG model fit more data variance than either of the Rossby wave models. Fundamentally, this was because the QG model offers more degrees of freedom than does the Rossby wave model. In essence the QG model allowed for a "richer" spectrum of waves in its interior flow field compared to the limited number of spectral coefficients offered by the Rossby wave model. Non-linear effects of the QG model may also have been a factor. The non-linear transfer of energy to the third baroclinic mode shown in Experiment E3 may have accounted for the QG model capturing more of the data variance.

E3 also indicated important differences between the time evolution of the waves that were fit using the Rossby wave model and the QG model. Although the spectrum of the baroclinic mode appeared similar in both model estimates, the barotropic mode had more temporal variability in the QG estimate. This may be attributed to the additional topography and the non-linear effects in the QG model. It would be useful in the future to examine these differences between the linear and non-linear fits more fully.

The RMS of the innovation sequence was considerably higher than the RMS of the residuals. This was likely due to mis-specifying the model errors,  $Q$ . Assumptions about the data and model errors are important factors in reducing the innovation sequence. For instance, underestimating  $Q$  could cause the forecast covariance to collapse and result in the measurements being ignored in the assimilation. Conversely, overestimating  $Q$  would cause the measurements to be weighted too heavily. A more preferable estimate for  $Q$  could be obtained

from a twin experiment run using the QG model itself.

This work is just the beginning of what could be accomplished with the AMODE data set. We have a stronger understanding of how to incorporate tomographic data into circulation models and the types of results one can expect. Further, we have gained insight into the usefulness of assimilating tomographic measurements into numerical models. There is great opportunity to extend this research to learn even more about the AMODE region and, at the same time, learn more about the subtleties of assimilating tomographic data into numerical models.

## BIBLIOGRAPHY

- Apel, J. (1987). *Principles of Ocean Physics*. Harcourt Brace Jovanovich.
- Bell, B. M. (1994). The iterated Kalman smoother as a Gauss–Newton method. *SIAM J. Optimization*, 4(3):626–636.
- Bennett, A. F. (1992). *Inverse Methods in Physical Oceanography*. Cambridge University Press.
- Charney, J., Fjortoft, R., and von Neumann, J. (1950). Numerical integration of the barotropic vorticity equation. *Tellus*, 2:237–254.
- Chiu, C.-S. and Desaubies, Y. (1987). A planetary wave analysis using the acoustic and conventional arrays in the 1981 Ocean Acoustic Tomography Experiment. *J. Phys. Oceanogr.*, 17:1270–1287.
- Cornuelle, B. (1983). *Inverse Methods and Results from the 1981 Ocean Acoustic Tomography Experiment*. PhD thesis, Woods Hole Oceanographic Institute.
- Cornuelle, B. (1996). Ocean acoustic tomography: Integral data and ocean models. In Malanotte-Rizzoli, P., editor, *Modern Approaches to Data Assimilation in Ocean Modeling*. Elsevier Science.
- Cornuelle, B. and Howe, B. (1987). High spatial resolution in vertical slice ocean acoustic tomography. *J. Geophys. Res.*, 92:11,680–11,692.
- Cornuelle, B., Munk, W., and Worcester, P. (1989). Ocean acoustic tomography from ships. *J. Geophys. Res.*, 94:6232–6250.
- Cornuelle, B., Wunsch, C., Behringer, D., Birdsall, T., Brown, M., Heinmiller, R., Knox, R., Metzger, K., Munk, W., Spiesberger, J., Spindel, R., Webb, D., and Worcester, P. (1985). Tomographic maps of the ocean mesoscale, I, Pure acoustics. *J. Phys. Oceanogr.*, 15:133–152.

- Dushaw, B., Chester, D., and Worcester, P. (1993). A review of ocean current and vorticity measurements using long-range reciprocal acoustic transmissions. In *OCEANS '93 Conference Record*, pages 298–305, Victoria, B.C.
- Dushaw, B. D., Worcester, P. F., Cornuelle, B. D., Marshell, A. R., Howe, B. M., Leach, S., Mercer, J. A., and Spindel, R. C. (1996). Data report: Acoustic mid-ocean dynamics experiment (AMODE). Technical report, Applied Physics Laboratory, University of Washington.
- Gaillard, F. (1992). Evaluating the information content of tomographic data: Application to mesoscale observations. *J. Geophys. Res.*, 97(C10):15,489–15,505.
- Haidvogel, D., Robinson, A., and Schulman, E. (1980). The accuracy, efficiency, and stability of three numerical models with application to open ocean problems. *J. Comput. Phys.*, 34:1–53.
- Hogg, N. G. (1996). Oceanographic data for parameter estimation. In Malanotte-Rizzoli, P., editor, *Modern Approaches to Data Assimilation in Ocean Modeling*. Elsevier Science B.V.
- Holland, W. and Capotondi, A. (1996). Recent developments in prognostic ocean modeling. In Malanotte-Rizzoli, P., editor, *Modern Approaches to Data Assimilation in Ocean Modeling*. Elsevier Science B.V.
- Howe, B. M., Worcester, P. F., and Spindel, R. C. (1987). Ocean acoustic tomography: Mesoscale velocity. *J. Geophys. Res.*, 92:3785–3805.
- Kak, A. and Slaney, M. (1988). *Principles of Computerized Tomographic Imaging*. IEEE Press, New York.
- Levitus, S. (1982). *NOAA Prof. Paper*, 13:173.
- Malanotte-Rizzoli, P. and Holland, W. R. (1986). Data constraints applied to models of the ocean general circulation, I, The steady case. *J. Phys. Oceanogr.*, 16:1665–1682.
- McWilliams, J. and Flierl, G. (1976). Optimal, quasi-geostrophic wave analysis for MODE array data. *Deep-Sea Res.*, 23:285–300.



- Miller, R., Robinson, A., and Haidvogel, D. (1983). A baroclinic quasi-geostrophic open ocean model. *J. Comput. Phys.*, 50:38–70.
- Miller, R. N. and Bennett, A. F. (1988). Numerical simulation of flows with locally characteristic boundaries. *Tellus*, 40A:303–323.
- Miller, R. N., Busalacchi, A. J., and Hackert, E. C. (1997). Applications of data assimilation to analysis of the ocean on large scales. *J. Met. Soc.*, 75:445–462.
- Munk, W., Worcester, P., and Wunsch, C. (1995). *Ocean Acoustic Tomography*. Cambridge University Press, 40 West 20th Street, New York, NY 10011-4211. 433 pp.
- Munk, W. and Wunsch, C. (1979). Ocean acoustic tomography: A scheme for large scale monitoring. *Deep-Sea Res.*, 26:123–161.
- Munk, W. and Wunsch, C. (1982). Observing the ocean in the 1990's. *Phil. Trans. Roy. Soc.*, A307:439–464.
- Pinardi, N. and Robinson, A. R. (1987). Dynamics of deep thermocline jets in the POLYMODE region. *J. Phys. Oceanogr.*, 17:1163–1188.
- Rienecker, M. M. and Miller, R. N. (1991). Ocean data assimilation using optimal interpolation with a quasi-geostrophic model. *J. Geophys. Res.*, 96(C8):15,093–15,103.
- Spiesberger, J. L., Bushong, P. J., Jr., K. M., and Birdsall, T. G. (1989). Basin-scale tomography: Synoptic measurements of a 4000-km length section in the Pacific. *J. Phys. Oceanogr.*, 19:1073–1090.
- The AMODE–MST Group (1994). Moving ship tomography in the North Atlantic. *EOS*, 75(2):17,21.
- The MODE Group (1978). The mid-ocean dynamics experiment. *Deep-Sea Res.*, (25):859–910.
- Worcester, P., Cornuelle, B., and Spindel, R. (1991). A review of ocean acoustic tomography: 1987–1990. *Reviews of Geophysics, U.S. National Report to International Union of Geodesy and Geophysics 1987–1990*, pages 557–570.

- Wunsch, C. (1983). Western north atlantic. In Robinson, A., editor, *Eddies in Marine Science*, pages 47–65. Springer-Verlag, Berlin.
- Wyrski, K., Mgaard, L., and Hager, J. (1976). Eddy energy in the oceans. *J. Geophys. Res.*, 81:2641–2646.

## VITA

Chris G. Walter

**Birth:**

24 January 1963 Kalispell, Montana

**Education:**

M.S. Geophysics, University of Washington, 1993

B.A. Geophysical Engineering, Montana College of Mineral Science and Technology

**Experience:**

**1997-Present:** Data Analyst, The Boeing Company, Seattle, WA.

**1989-Present:** Masters and Ph.D. Candidate, Applied Physics Laboratory/University of Washington, Seattle, WA.

**1995-1997:** Software Consultant, Williamson and Associates, Seattle, WA

**1985-1989:** Exploration Geophysicist, Tenneco Oil Exploration and Production, Houston, TX.

**1984-1985:** Field Geophysicist, Western Geophysical, Chateau, AT.

**PUBLICATIONS:**

- C.G. Walter. Towed tomography data from the gulf stream. Master's thesis, University of Washington, 1993. 45pp.
- The Acoustic Mid-Ocean Dynamics Experiment Group. Moving ship tomography in North Atlantic. EOS, 75(2);17,21, 1994.

**REPORT DOCUMENTATION PAGE**Form Approved  
OPM No. 0704-0188

Public reporting burden for this collection of information is estimated to average 1 hour per response, including the time for reviewing instructions, searching existing data sources, gathering and maintaining the data needed, and reviewing the collection of information. Send comments regarding this burden estimate or any other aspect of this collection of information, including suggestions for reducing this burden, to Washington Headquarters Services, Directorate for Information Operations and Reports, 1215 Jefferson Davis Highway, Suite 1204, Arlington, VA 22202-4302, and to the Office of Information and Regulatory Affairs, Office of Management and Budget, Washington, DC 20503.

<b>1. AGENCY USE ONLY (Leave blank)</b>		<b>2. REPORT DATE</b> July 2000	<b>3. REPORT TYPE AND DATES COVERED</b> Technical	
<b>4. TITLE AND SUBTITLE</b>  Data Assimilation for Ocean Acoustic Tomography			<b>5. FUNDING NUMBERS</b>  N00014-97-1-0259	
<b>6. AUTHOR(S)</b>  Chris G. Walter				
<b>7. PERFORMING ORGANIZATION NAME(S) AND ADDRESS(ES)</b> Applied Physics Laboratory University of Washington 1013 NE 40th Street Seattle, WA 98105-6698			<b>8. PERFORMING ORGANIZATION REPORT NUMBER</b>  APL-UW TR 9901	
<b>9. SPONSORING / MONITORING AGENCY NAME(S) AND ADDRESS(ES)</b> Office of Naval Research Jeff Simmens, Code ONR 321OA 800 North Quincy Street Arlington, VA 22217-5660			<b>10. SPONSORING / MONITORING AGENCY REPORT NUMBER</b>	
<b>11. SUPPLEMENTARY NOTES</b>				
<b>12a. DISTRIBUTION / AVAILABILITY STATEMENT</b>  Approved for public release; distribution is unlimited.			<b>12b. DISTRIBUTION CODE</b>	
<b>13. ABSTRACT (Maximum 200 words)</b>  This research evaluates the effectiveness of assimilating ocean acoustic tomography data into numerical ocean models. Acoustic tomography uses sound to remotely sample integrated or averaged properties of the ocean. These properties include soundspeed and current velocity. Three different models are used in the assimilation: 1) a linear Rossby wave model without advection, 2) a Rossby wave model with advection, and 3) a non-linear quasi-geo strophic model. We examine the tomographic data's effectiveness by assimilating non-averaging point measurements, such as temperature data, and integral data with the Rossby wave model. First, simulated data are used in benchmark experiments. These are followed by a second series of experiments in which actual tomographic data collected during the Acoustic Mid-Ocean Dynamics Experiment (AMODE) are used. We compare the value of the integral measurements in terms of forecasting accuracy in both physical and spectral space. Although both forms of data constrain the model equally as well in an average sense (the number of data were chosen to do this), the tomographic data are found to constrain low wavenumber components of the model more accurately. Differences between the model estimates and data are within expected error bars. These error bars are based on prior statistical assumptions about errors in the model and observations, boundary conditions and initial conditions. The Rossby wave models with and without advection account for 62.1% and 60.7% of the data variance respectively and the quasi-geostrophic model accounts for 66.0% of the variance. The purpose of this research is not to evaluate any particular numerical model, but rather to better understand the usefulness of assimilating tomographic measurements into numerical models.				
<b>14. SUBJECT TERMS</b>  data assimilation, Kalman filtering, ocean acoustic tomography, ocean circulation modeling, AMODE			<b>15. NUMBER OF PAGES</b>  76	
			<b>16. PRICE CODE</b>	
<b>17. SECURITY CLASSIFICATION OF REPORT</b>  Unclassified	<b>18. SECURITY CLASSIFICATION OF THIS PAGE</b>  Unclassified	<b>19. SECURITY CLASSIFICATION OF ABSTRACT</b>  Unclassified	<b>20. LIMITATION OF ABSTRACT</b>  SAR	